

**Current-Induced Transition from Particle-by-Particle to Concurrent Intercalation in  
Phase-Separating Battery Electrodes**

Yiyang Li<sup>1</sup>, Farid El Gabaly<sup>2</sup>, Todd R. Ferguson<sup>3</sup>, Raymond B. Smith<sup>3</sup>, Norman C. Bartelt<sup>2</sup>,  
Joshua D. Sugar<sup>2</sup>, Kyle R. Fenton<sup>4</sup>, Daniel A. Cogswell<sup>5</sup>, A. L. David Kilcoyne<sup>6</sup>,  
Tolek Tyliczszak<sup>6</sup>, Martin Z. Bazant<sup>3,7</sup>, William C. Chueh<sup>1,8,\*</sup>

<sup>1</sup>Department of Materials Science & Engineering, Stanford University, Stanford, CA 94305

<sup>2</sup>Sandia National Laboratories, Livermore, CA 94551

<sup>3</sup>Department of Chemical Engineering, Massachusetts Institute of Technology, Cambridge, MA  
02139

<sup>4</sup>Sandia National Laboratories, Albuquerque, NM 87185

<sup>5</sup>Samsung Advanced Institute of Technology America, Cambridge, MA 02142

<sup>6</sup>Advanced Light Source, Lawrence Berkeley National Laboratory, Berkeley, CA 94720

<sup>7</sup>Department of Mathematics, Massachusetts Institute of Technology, Cambridge, MA 02139

<sup>8</sup>Stanford Institute of Materials and Energy Science, Menlo Park, CA 94025

\*Corresponding Author, [wchueh@stanford.edu](mailto:wchueh@stanford.edu)

**Abstract:** Many battery electrodes contain ensembles of nanoparticles that phase-separate upon (de)intercalation. In such electrodes, the fraction of actively-intercalating particles directly impacts cycle life: a vanishing population concentrates the current in a small number of particles, leading to current hotspots. Reports on the active particle population in the phase-separating electrode lithium iron phosphate (LFP) vary widely, ranging from around 0% (particle-by-particle) to 100% (concurrent intercalation). Using synchrotron-based X-ray microscopy, we probed the individual state-of-charge for over 3,000 LFP particles. We observed that the active population depends strongly on the cycling current, exhibiting particle-by-particle-like behaviour at low rates and increasingly concurrent behaviour at high rates, consistent with our phase-field porous electrode simulations. Contrary to intuition, the current density, or current per active internal surface area, is nearly invariant with the global electrode cycling rate. Rather, the electrode accommodates higher current by increasing the active particle population. This behaviour results from thermodynamic transformation barriers in LFP, and such a phenomenon likely extends to other phase-separating battery materials. We propose that modifying the transformation barrier and exchange current density can increase the active population and thus the current homogeneity. This could introduce new paradigms to enhance the cycle life of phase-separating battery electrodes.

Electrochemical systems can provide clean and efficient routes for energy conversion and storage. Many electrochemical devices such as batteries, fuel cells, and supercapacitors consist of porous electrodes containing ensembles of nanoparticles<sup>1</sup>. For typical microstructures, the particle density can reach as high as  $10^{15} \text{ cm}^{-3}$ . To further increase complexity, many intercalation battery electrodes, such as graphite<sup>2</sup>, lithium iron phosphate<sup>3,4</sup>, lithium titanate<sup>5</sup>, and spinel lithium nickel manganese oxide<sup>6</sup>, phase-separate upon (de)intercalation. Such electrodes are physically and chemically heterogeneous on the nanoscale, and likely exhibit inhomogeneous current distributions.

In phase-separating electrodes, the active particle population is a crucial factor in determining the overall electrode current and the degree of current homogeneity. The electrode current is given by:

$$I = \sum_n A_n j_n \approx A \bar{j} X \quad (1)$$

where  $A_n$  is the reaction area of the  $n^{\text{th}}$  actively-intercalating particle, and  $j_n$  is the current density of that particle. Under the approximation of similar particle size, we obtain the final expression in equation 1, where  $\bar{j}$  is the average current density of all actively-intercalating particles,  $A$  is the total internal surface area of all particles (rather than the projected electrode area), and  $X$  is the so-called active population. When  $X$  approaches 0%, the electrode intercalates particle-by-particle with a heterogeneous current distribution; when  $X$  approaches 100%, the electrode intercalates concurrently with a more homogeneous current distribution.

The active population impacts the electrode's cycle life because it is directly related to the local current density. For example, with a small active population, the electrochemical current is concentrated in a small number of particles, leading to high local current densities and

current hotspots that could induce fracture and accelerate capacity fading<sup>7,8</sup>. Thus, from an electrode engineering perspective, increasing the active population could improve cycle life. On a fundamental level, the active population also affects the fidelity of electrochemical parameters, such as those extracted from electrochemical impedance spectroscopy and potentiostatic intermittent titration.

Lithium iron phosphate ( $\text{LiFePO}_4$ , LFP) is a well-established model system for investigating lithium intercalation in phase-separating nanoparticles. At room temperature, moderately-sized ( $> 50$  nm) LFP particles phase-separate with a negligible solubility of the end-member phases<sup>3,9-11</sup>. Despite being one of the most intensely studied positive battery electrodes, there exist disagreements about the non-equilibrium intercalation pathway of Li in LFP<sup>12</sup>. A seemingly contradictory observation is the fraction of actively-intercalating particles, with reports ranging from around 0% (particle-by-particle)<sup>13-17</sup> to 100% (concurrent intercalation)<sup>18,19</sup>. Such discrepancies remain to be reconciled. On the one hand, the so-called “mosaic” particle-by-particle intercalation mechanism has been reported in studies using X-ray diffraction<sup>13</sup>, electron microscopy<sup>14,15</sup>, and X-ray microscopy<sup>16</sup>. Dreyer *et al.* proposed that the thermodynamic origin of this behaviour arises from the non-monotonic chemical potential of Li as a function of the particle’s composition<sup>17</sup>. On the other hand, a concurrent intercalation pathway, whereby most particles intercalate at once, has also been observed in LFP<sup>18,19</sup>.

Despite its crucial importance, the active population has been largely neglected in models describing electrode cycling<sup>20-23</sup>. Differing approximations in the active population may have contributed to the vast range of experimentally-measured specific exchange current densities, which range from  $10^{-6}$  A m<sup>-2</sup> to  $10^{-1}$  A m<sup>-2</sup> in LFP<sup>20-23</sup>. The active population has sometimes been considered in terms of an electrode-level lithiation front from the separator to the current

collector<sup>24</sup>. Bai and Tian recently proposed an active particle population model based on nucleation and growth<sup>25</sup>, which has been used to interpret current transients of an electrode under potentiostatic conditions<sup>26,27</sup>.

In this work, we employed synchrotron-based scanning transmission X-ray microscopy (STXM) to capture snapshots of the state-of-charge (SoC) of individual LFP particles in electrodes cycled at rates between C/50 and 5.0 C (C indicates the rate it takes to charge or discharge the electrode in 1 h). Using techniques established in our previous work<sup>16</sup>, we analysed the SoC of individual particles for over 3,000 particles at a spatial resolution of  $\sim 28$  nm. During charge, we observed that only 5 to 8 % of particles are actively-intercalating. Conversely, during discharge, the active population is highly rate-dependent and ranges from 8 to 32 %. Our results show unambiguously that the active population depends strongly on the cycling condition and displays an increasingly concurrent behaviour at higher rates of discharge. As such, the intercalation pathway is not a static property of the electrode, but rather a dynamic one. **The active particle behaviour cannot be inferred from macroscopic current-voltage measurements.** We used a modified porous electrode model<sup>24</sup>, which combines porous electrode theory<sup>28</sup> with phase-field electrochemical thermodynamics<sup>29</sup>, to simulate the lithium intercalation behaviour for a 100-particle electrode. We show that the actively-intercalating population is determined by the competition between a transformation barrier and the reaction overpotential needed to (de)lithiate the particles at a given rate. Such insights suggest new pathways toward increasing the current homogeneity in battery electrodes.

To prepare experimental samples, we electrochemically cycled coin-cell batteries containing a  $\sim 60$ - $\mu\text{m}$ -thick LFP positive electrode, fabricated from commercial carbon-coated powder with an average particle size of 230 nm (see Methods and Supplementary section 1).

After five formation cycles, we (dis)charged the batteries to the desired SoC, rapidly disassembled them in a dry room or in an Ar-filled glovebox, and rinsed the electrodes with excess dimethyl carbonate. The disassembly process was completed in 4 minutes after terminating the current, except for the electrode discharged at a rate of C/50, which was completed in 10 minutes. By removing the electrolyte faster than the (dis)charging time, we minimized inter-particle lithium transport. As we will show later, a strong dependence of the active particle population on the cycling condition confirms that we preserved the electrode's non-equilibrium behaviour. Finally, we used an ultramicrotome to cross-section the electrodes into  $\sim 300$  nm-thick strips, each containing one to two particles along the thickness of the cross-section.

We imaged three to four  $5 \times 5$   $\mu\text{m}$  regions at different positions along the thickness of each electrode using the STXM at beam line 11.0.2<sup>30</sup> in the Advanced Light Source (with preliminary measurements done at beam line 5.3.2<sup>31,32</sup>). We raster-scanned the nanosized X-ray beam while varying the photon energy across the Fe  $L_3$  absorption edge. The single-pixel SoC is calculated by fitting a linear combination of the  $\text{LiFePO}_4$  and  $\text{FePO}_4$  reference spectra (Fig. 1a) to the single-pixel X-ray absorption spectra. As shown recently, the spectroscopically-determined SoC is comparable to the electrochemically-determined ones<sup>16,33</sup>. We also confirmed that fully-charged and fully-discharged electrodes indeed contain only the respective end-member phase (Fig. S5), indicating that the entire battery electrode is being cycled. Figure 1b shows a typical SoC map for a region in an electrode. The hue at each pixel represents the SoC, with red as fully lithiated (discharged) and green as fully delithiated (charged). The brightness, on the other hand, represents the particle thickness at each pixel.

Before analysing the SoC for individual LFP particles, we averaged the pixels to obtain the mean SoC as a function of the distance from the current collector (Fig. S6). A sharp lithiation front was not detected along the thickness of the electrode, although we observed a small preference for LFP particles near the separator/electrode interface to be delithiated in electrodes charged at higher rates, and vice versa for discharge. This suggests a small Li ion concentration gradient in the electrolyte. To identify particle boundaries as well as overlapped particles, we employed TEM to image the same region in each LFP electrode (Fig. 1c). Figures 1d-f show typical LFP particles and the corresponding Fe L<sub>3</sub> absorption spectra averaged over the particles. The linear combination analysis, which was employed to determine the SoC of the particles, yielded excellent fits.

We analysed the total lithium content within individual particles in six different electrodes, each cycled at a different rate. An LFP particle with a SoC between 20-80% is considered actively-intercalating. By defining active particles as being within the coherent solubility limit<sup>34</sup>, we minimize the misidentification of active particles due to the insufficient signal-to-noise of smaller particles and around particle boundaries. Unlike previous work, our definition does not rely on observing phase boundaries<sup>14,18</sup>, as they would not be observed during solid-solution filling<sup>35-37</sup>, nor if they lie perpendicular to the X-ray beam. Sensitivity analysis confirmed that our conclusions are qualitatively independent of the single-particle SoC thresholds (Fig. S8-9). The active particles are outlined in select SoC maps and TEM images (Figs 1b-c and S4). The single-particle SoC analysis confirms that a porous LFP electrode is chemically heterogeneous during cycling: lithium-rich, lithium-poor, and actively-intercalating particles coexist in the same electrode.

Figure 2 shows the fraction of actively-intercalating particles in each electrode as a function of charge and discharge rates at a nominally 50% electrode SoC (see Fig. S4 for corresponding SoC maps). For all charging rates between 1.0 C and 5.0 C, the actively-intercalating population ranged from 5 to 8 %, indicating that the LFP ensemble proceeds closely to the particle-by-particle pathway. In other words, the time required to charge individual active particles is a factor of 12-20 less than the electrode charging time. Our results confirm that current is heterogeneously distributed in the electrode: a small number of active particles carry most of the current, regardless of the total electrode charging current. In contrast, on discharge, the actively-intercalating population showed a significant dependence on the rate. Specifically, at a rate of 5.0 C, the actively-intercalating fraction upon discharge (32%) is more than 6 times that during charge (5%). While the active particle fraction varies somewhat across the thickness of the electrode (Fig. S7), the active population of any region in a 5.0 C discharge electrode is clearly larger than that of any other cycling condition.

Summarizing the experimental findings, we observed the onset of a transition between particle-by-particle and concurrent intercalation on discharge. In contrast, all charge rates yielded particle-by-particle-like intercalation behaviour. Based on Eq. 1, the local current density of actively-intercalating particles is higher upon charge than discharge. Such asymmetry is not easily observed in current-voltage measurements because the same reaction overpotential can yield different anodic and cathodic current densities. Our data suggest that the current homogeneity is not only dependent on the cycling rate but also on the direction (i.e., charge vs. discharge). By showing that the active population of an LFP electrode depends strongly on the cycling condition, our experiments reconcile the seemingly contradictory reports of particle-by-particle<sup>13-17</sup> and concurrent intercalation pathways<sup>18,19</sup>: the differing experimental observations



result from different sample preparation routes. Fast, chemically delithiated particles, where the complete delithiation occurs within 2 minutes<sup>38</sup>, resulted in concurrent intercalation, while electrochemically-prepared samples at lower rates resulted in particle-by-particle intercalation.

Next, to understand the origins of the observed heterogeneous current distribution and the transition in the active population dynamics, we simulated the lithium distribution inside 100 particles under constant current cycling using a combined phase-field and porous electrode model<sup>24,29</sup>, illustrated schematically in Fig. 3. We assume that the local rate of (de)lithiation for a particle is limited by the surface reaction rather than by solid-state diffusion, consistent with previous work<sup>24,27,29,36</sup>. To describe the diffusional chemical potential, or the derivative of free energy with respect to composition<sup>39,40</sup>, we employed a one-dimensional Cahn-Hilliard regular solution model with an approximate description of coherency strain<sup>34,41</sup>:

$$\mu_{Li,LFP} = \Omega_a(1 - 2\tilde{c}_s) + k_B T \ln\left(\frac{\tilde{c}_s}{1 - \tilde{c}_s}\right) - \frac{\kappa}{\rho_s} \nabla^2 \tilde{c}_s + \frac{B_0}{\rho_s} (\tilde{c}_s - \bar{c}_s) \quad (2)$$

where  $\Omega_a$  is the regular solution parameter,  $\kappa$  is the gradient penalty from the Cahn-Hilliard equation,  $B_0$  is the coherent stress penalty,  $\rho_s$  is the lithium site concentration,  $\tilde{c}_s$  is the spatially-resolved lithium concentration in the solid normalized to the number of Li sites,  $\bar{c}_s$  is the average filling fraction of the particle, and  $k_B$  and  $T$  have the usual meanings. The composition-dependent  $\mu_{Li,LFP}$  has roughly the same shape upon charge and discharge in this model<sup>34</sup>. Next, we generalize Butler-Volmer kinetics<sup>29</sup> to describe the Li insertion rate consistently with the Cahn-Hilliard model:

$$J = k_0 \frac{a_{Li,yte}^{1-\alpha} a_{Li,s}^\alpha}{\gamma_{TS}} \left[ \exp\left(-\frac{\alpha e \eta}{k_B T}\right) - \exp\left(\frac{(1-\alpha) e \eta}{k_B T}\right) \right] \quad (3)$$

where  $k_0$  is the rate constant,  $a_{Li,s}$  and  $a_{Li,yte}$  are the respective activities of lithium in the solid particles and in the electrolyte,  $e$  is the elementary charge,  $\eta$  is the reaction overpotential at the LFP/carbon/electrolyte triple-phase boundary, and  $\gamma_{TS}$  is the activity coefficient of the transition state representing excluded sites. We use  $\alpha$  as a phenomenological parameter to capture the experimentally-observed asymmetry between charge and discharge. Such an asymmetry may also result from an asymmetry in  $\mu_{Li,LFP}$ <sup>37</sup> or in kinetic parameters<sup>42–44</sup>. We neglect deviations from Butler-Volmer kinetics at high reaction overpotentials that has recently been observed in LFP<sup>27</sup>. Finally, we consider ionic diffusion and migration losses at the porous electrode level (Eqs. S1-5). **The model neglects microscopic variations in the electrode in the plane of the current collector. Because transport in the electrolyte is fast (Fig. S6), such variations should not yield significant deviations in the intercalation behaviour of the porous electrode investigated in this work.** See Supplementary section 5 for details of the model.

We fit the active particle population predicted by the model to the experimental results, with  $k_0$  and  $\alpha$  as fitting parameters (Fig. 2). We obtain good fits, with an  $\alpha$  of 0.2 and a  $k_0$  of 0.6 A m<sup>-2</sup>, yielding an average exchange current density of  $\sim 0.3$  A m<sup>-2</sup>. The exchange current density is higher than most reported values in literature; however, past work did not consider the active particle fraction and likely overestimated the active reaction area<sup>20–23</sup>. The fittings may also be affected by departures from Butler-Volmer kinetics at high rates that that lead to curved Tafel plots and small effective values of  $\alpha$ <sup>27</sup>. Figure 4a plots the active particle population and active particle current density as a function of discharging rate. Due to high current densities (Fig. 4a), the model predicts solid-solution-like filling within a particle, consistent with previous simulations<sup>24,36</sup>. The corresponding SoC maps are shown in Fig. 4b-e.

Several important insights arise from our experiments and simulations. For discharge rates up to 5.0 C, we observed experimentally that the active particle population increases with rate, which is also captured in our simulations (Fig. 4a-c). In other words, the LFP electrode accommodates the increased current by increasing the active population. The current density of active particles is nearly invariant with the discharge rate in the simulations (Fig. 4a). Above a simulated discharge rate of 10 C, the active population saturates, but does not reach 100% because our active particle definition (between 20-80% SoC) is smaller than the miscibility gap of LFP. We define  $I_{\text{crit}}$  as the critical current at which 65% of particles are active; above  $I_{\text{crit}}$ , the current density increases significantly with the discharge rate (Fig. 4a).

We explain the above results using the presence of transformation barriers in LFP, and broadly in phase-separating electrodes. Figure 5a shows the diffusional chemical potential of Li ( $\mu_{\text{Li,LFP}}$ ) in a typical particle upon lithiation;  $\mu_{\text{Li,LFP}}$  contains a local maxima (transformation barrier,  $\Delta \mu_b$ ) at the composition  $\text{Li}_b\text{FePO}_4$ . In these simulations, we take the transformation barrier to be equal upon charge and discharge, where asymmetry is accounted for phenomenologically through  $\alpha$ . When the electrode ensemble potential lies below the transformation barrier, the particle cannot lithiate past  $\text{Li}_b\text{FePO}_4$  and does not activate. When the electrode ensemble potential nears the top of the transformation barrier (at the blue dashed line), some particles activate and lithiate further. The particles that do not activate sustain the electrode ensemble potential near the top of the transformation barrier. The driving force (i.e., reaction overpotential) for lithium insertion past composition  $\text{Li}_b\text{FePO}_4$  is the difference between the top of the transformation barrier (blue dashed line) and  $\mu_{\text{Li,LFP}}$  (black line).

Figure 5b plots the simulated reaction overpotential and the corresponding current density of a typical active particle. In regime 1, both quantities are approximately constant with rate: while the global discharge rate increases by a factor of 20, the reaction overpotential and current density increases by less than 50%. The slow increase in reaction overpotential with discharge rate in regime 1 arises from electrolyte transport losses and variations in particle size. The active population is determined by the average time needed to fill or empty a particle at a reaction overpotential ( $\eta_1$ ) approximately equal to the transformation barrier height ( $\Delta \mu_b/e$ ). This results in a high current density for each active particle, even at vanishing rates of discharge, in accordance with Eq. 1. The system responds to an increased current by increasing the number of actively-intercalating particles (Fig. 4a).

In regime 2, where the electrode current exceeds  $I_{\text{crit}}$ , the electrode attains concurrent intercalation, and the active particle population saturates. In other words, the surface area available for intercalation in the electrode is maximized. Raising the reaction overpotential above  $\Delta \mu_b/e$  (to  $\eta_2$ , purple dotted lines in Fig. 5a) does not further increase the particles' activation rate. Instead, the additional reaction overpotential beyond  $\Delta \mu_b/e$  increases the particles' current density (Figs 4a and 5b). At extremely high rates,  $\Delta \mu_b/e$  becomes insignificant compared to the reaction overpotential.

Within regime 1, our simulations also predict the experimentally observed asymmetry in the active particle population between charge and discharge. During charging, the current density  $j_n$  of an active particle is high due to the phenomenological parameter  $\alpha$ , resulting in a large Li intercalation rate at a reaction overpotential  $\eta_1$  equal to  $\Delta \mu_b/e$ . In contrast, the same overpotential yields a much smaller current density under discharge. The asymmetry in the active

particle population is not necessarily reflected in the galvanostatic voltage profiles—the same reaction overpotential magnitude can result in different anodic and cathodic current densities, and thus an asymmetry in the active particle population in accordance with Eq. 1.

As evident in the above discussions, the active population dynamics in LFP result from the transformation barriers, which arise from the diffusional chemical potential. While our phase-field simulations predict solid-solution-like particles, we observe the same active particle dynamics for phase-separating particles in the absence of coherency strain (Fig. 4a). Modifying the transformation barrier height yields similar transitions between particle-by-particle and concurrent intercalation (Fig. S11), suggesting that such active particle dynamics likely extend to other phase-separating materials. For all simulated conditions, we observe large current densities even at vanishing rates of discharge.

Our simulations also suggest that the reaction overpotential should be weakly dependent on the discharge rate in regime 1 (Fig. 5b). The experimentally measured voltage, however, shows a strong Ohmic-like dependence (Figs S3 and S10). Low percolation of the carbon network (with a technologically-relevant carbon loading of 6 wt%) likely leads to weakly-connected patches in the electrode that rely on interparticle contact resistance for electronic transport<sup>22</sup>, resulting in the observed Ohmic resistance. The sequence in which particles (de)lithiate is determined by their distance from the closest carbon network (Fig. S13a) rather than by the distance from the current collector or separator, consistent with Fig. S6. Indeed, increasing the carbon loading to 20 wt% strongly suppressed the voltage's dependence on cycling rate (Fig. S10). Using our phase-field model, we examined the effect of electronic wiring<sup>45</sup> on the active population dynamics. The simulation (Fig. S13) confirms that the qualitative features of the observed active particle dynamics are not significantly affected by

wiring. Therefore, while wiring contributes significantly to the measured voltage, it alone cannot lead to the active particle dynamics observed in the experiments. Similarly, we also show that electrochemical heterogeneities do not significantly alter the qualitative behaviour of the active population (Fig. S14).

From an electrode engineering perspective, the cycling rate is an important factor in determining the cycle life of Li-ion batteries, as high current densities result in current hotspots and electromechanical shocks and fractures<sup>7,8</sup>. However, it is not the global cycling rate, but the local current per active surface area that determines the extent of shocks and fractures. Because the local current density is not easily determined by macroscopic current and voltage measurements, the global cycling rate is commonly used in its place in conjunction with a homogeneous electrode or an electrode-transport-limited assumption (Fig. 6). Our results demonstrate that the local current density can be high for active particles even when the global electrode cycling rate is low (Figs 4a and 5b), a result of the transformation barrier in phase-separating electrodes. Thus, using the global cycling rate to predict the local cycling rate can lead to erroneous predictions (Fig. 6).

Enhancing cycle life by reducing the local current density may come from increasing the active population and more evenly distributing the current. Our work suggests that a potentially viable method is to decrease the transformation barrier height ( $\Delta\mu_b$ ). As we have shown earlier, the reaction overpotential is approximately equal to  $\Delta\mu_b$  in regime 1. Thus, at a given cycling rate, a lower barrier reduces the local current density, increases the active particles fraction, and improves the current homogeneity (Fig. S11). There is growing evidence that the transformation barrier height can be controlled by nanostructuring and chemical modifications. For instance, the nucleation barrier in a phase-separating material was shown to be inversely proportional to the

surface area to volume ratio of the nanoparticles<sup>34</sup>. Additionally, Nb doping<sup>46</sup> and V substitution<sup>47</sup> in LFP reduce the lattice mismatch and increase the solubility limits, both strong indicators of decreased transformation barrier. Mn substitution in LiFePO<sub>4</sub>, on the other hand, has been shown to eliminate the nucleation barrier and result in extensive solid solubility upon lithiation<sup>48</sup>. Yet another somewhat counter-intuitive route is to lower the reaction rate  $k_0$  and exchange current density, which would increase the active particle population. Our results suggest that modifying the reaction rate, such as through surface coating<sup>49</sup>, surface modification<sup>50</sup>, and electrolyte additives could be used to control the active particle population and current homogeneity. We note, however, that the lower reaction rate may increase the electrode energy dissipation.

In summary, by analysing the individual state-of-charge of over 3,000 LFP particles cycled at different rates, we observed that the fraction of active particles is highly dependent on cycle rate and direction. The contradictory reports of particle-by-particle and concurrent intercalation pathways can be reconciled by considering the different electrochemical conditions. By combining experimental observation with phase-field simulations, we show that the active particle population is governed by the competition between a thermodynamic transformation barrier and the reaction overpotential needed to insert or extract lithium. Contrary to intuition, the current density, or current per active internal surface area, is nearly invariant with the global electrode cycling rate under typical cycling conditions, and even low rates of charge and discharge can produce high local current densities. Such behaviour likely occurs in other phase-separating battery materials that contain a transformation barrier. We propose that increasing the active population, through strategies like manipulating the transformation barrier and exchange

current density, can improve current uniformity and cycle life in phase-separating battery electrodes.



## Methods & Materials

For state-of-charge imaging experiments, the electrodes consist of 88 wt% carbon-coated LFP (Mitsui Engineering Shipbuilding Co. Ltd, particle size distribution shown in Fig. S1), 6 wt% polyvinylidene fluoride (PVDF), and 6 wt% Shawinigan acetylene black carbon. PVDF was first dissolved in N-methyl-2-pyrrolidone. LFP and carbon black were added to the slurry to obtain a viscosity of  $\sim 200$  cP. The slurry was then cast onto a carbon-coated aluminium current collector using a reverse comma coater. Solvent was dried at  $100^\circ\text{C}$  in ambient and subsequently dried under vacuum at  $100^\circ\text{C}$  for  $\sim 12$  h. The electrode mass loading and thickness were  $\sim 9$  mg  $\text{cm}^{-2}$  and  $60$   $\mu\text{m}$ , respectively. Finally, the LFP electrode was assembled in a 2032 coin cell, which consisted of a Li anode, a  $50$   $\mu\text{m}$  Tonen separator, and  $1.2$  M  $\text{LiPF}_6$  in 3:7 (wt/wt) ethylene carbonate: ethyl methyl carbonate electrolyte.

We performed five charge (C/12) and discharge (C/6) formation cycles. The termination voltages were  $3.8$  V for charge and  $2.5$  V for discharge. A stable capacity of  $\sim 150$  mAh  $\text{g}^{-1}$  was attained. For subsequent charging and discharging, the rates were calculated by the actual capacity. Figure S2 shows the typical charging and discharging curves at low rates, and Fig. S3 shows the curves for partially-charged and partially-discharged electrodes used in the SoC imaging experiments.

For more information on X-ray image analysis and phase-field modelling, see the Supplementary Information.

## References

1. Aricò, A. S., Bruce, P., Scrosati, B., Tarascon, J.-M. & Van Schalkwijk, W. Nanostructured materials for advanced energy conversion and storage devices. *Nature Mater.* **4**, 366–377 (2005).
2. Ohzuku, T., Iwakoshi, Y. & Sawai, K. Formation of Lithium-Graphite Intercalation Compounds in Nonaqueous Electrolytes and Their Application as a Negative Electrode for a Lithium Ion (Shuttlecock) Cell. *J. Electrochem. Soc.* **140**, 2490–2498 (1993).
3. Padhi, A. K., Nanjundaswamy, K. S. & Goodenough, J. B. Phospho-olivines as Positive-Electrode Materials for Rechargeable Lithium Batteries. *J. Electrochem. Soc.* **144**, 1188–1194 (1997).
4. Tang, M., Carter, W. C. & Chiang, Y.-M. Electrochemically Driven Phase Transitions in Insertion Electrodes for Lithium-Ion Batteries: Examples in Lithium Metal Phosphate Olivines. *Annu. Rev. Mater. Res.* **40**, 501–529 (2010).
5. Ohzuku, T., Ueda, A. & Yamamoto, N. Zero-Strain Insertion Material of  $\text{Li}[\text{Li}_{1/3}\text{Ti}_{5/3}]\text{O}_4$  for Rechargeable Lithium Cells. *J. Electrochem. Soc.* **142**, 1431–1435 (1995).
6. Ariyoshi, K., Iwakoshi, Y., Nakayama, N. & Ohzuku, T. Topotactic Two-Phase Reactions of  $\text{Li}[\text{Ni}_{1/2}\text{Mn}_{3/2}]\text{O}_4$  ( $\text{P4}_332$ ) in Nonaqueous Lithium Cells. *J. Electrochem. Soc.* **151**, A296–A303 (2004).
7. Woodford, W. H., Chiang, Y.-M. & Carter, W. C. “Electrochemical Shock” of Intercalation Electrodes: A Fracture Mechanics Analysis. *J. Electrochem. Soc.* **157**, A1052–A1059 (2010).
8. Christensen, J. & Newman, J. Stress generation and fracture in lithium insertion materials. *J. Solid State Electrochem.* **10**, 293–319 (2006).
9. Yamada, A. *et al.* Room-temperature miscibility gap in  $\text{Li}_x\text{FePO}_4$ . *Nature Mater.* **5**, 357–360 (2006).
10. Meethong, N., Huang, H.-Y. S., Carter, W. C. & Chiang, Y.-M. Size-Dependent Lithium Miscibility Gap in Nanoscale  $\text{Li}_{1-x}\text{FePO}_4$ . *Electrochem. Solid-State Lett.* **10**, A134–A138 (2007).
11. Wagemaker, M. *et al.* Dynamic Solubility Limits in Nanosized Olivine  $\text{LiFePO}_4$ . *J. Am. Chem. Soc.* **133**, 10222–10228 (2011).
12. Malik, R., Abdellahi, A. & Ceder, G. A Critical Review of the Li Insertion Mechanisms in  $\text{LiFePO}_4$  Electrodes. *J. Electrochem. Soc.* **160**, A3179–A3197 (2013).

13. Delmas, C., Maccario, M., Croguennec, L., Le Cras, F. & Weill, F. Lithium deintercalation in LiFePO<sub>4</sub> nanoparticles via a domino-cascade model. *Nature Mater.* **7**, 665–671 (2008).
14. Brunetti, G. *et al.* Confirmation of the Domino-Cascade Model by LiFePO<sub>4</sub>/FePO<sub>4</sub> Precession Electron Diffraction. *Chem. Mater.* **23**, 4515–4524 (2011).
15. Sugar, J. D. *et al.* High-resolution chemical analysis on cycled LiFePO<sub>4</sub> battery electrodes using energy-filtered transmission electron microscopy. *J. Power Sources* **246**, 512–521 (2014).
16. Chueh, W. C. *et al.* Intercalation Pathway in Many-Particle LiFePO<sub>4</sub> Electrode Revealed by Nanoscale State-of-Charge Mapping. *Nano Lett.* **13**, 866–872 (2013).
17. Dreyer, W. *et al.* The thermodynamic origin of hysteresis in insertion batteries. *Nature Mater.* **9**, 448–453 (2010).
18. Laffont, L. *et al.* Study of the LiFePO<sub>4</sub>/FePO<sub>4</sub> Two-Phase System by High-Resolution Electron Energy Loss Spectroscopy. **152**, 5520–5529 (2006).
19. Badi, S.-P. *et al.* Direct synthesis of nanocrystalline Li<sub>0.90</sub>FePO<sub>4</sub>: observation of phase segregation of anti-site defects on delithiation. *J. Mater. Chem.* **21**, 10085–10093 (2011).
20. Srinivasan, V. & Newman, J. Discharge Model for the Lithium Iron-Phosphate Electrode. *J. Electrochem. Soc.* **151**, A1517–A1529 (2004).
21. Yu, D. Y. W., Donoue, K., Inoue, T., Fujimoto, M. & Fujitani, S. Effect of Electrode Parameters on LiFePO<sub>4</sub> Cathodes. *J. Electrochem. Soc.* **153**, A835–A839 (2006).
22. Dargaville, S. & Farrell, T. W. Predicting Active Material Utilization in LiFePO<sub>4</sub> Electrodes Using a Multiscale Mathematical Model. *J. Electrochem. Soc.* **157**, A830–A840 (2010).
23. Prada, E. *et al.* Simplified Electrochemical and Thermal Model of LiFePO<sub>4</sub>-Graphite Li-Ion Batteries for Fast Charge Applications. *J. Electrochem. Soc.* **159**, A1508–A1519 (2012).
24. Ferguson, T. R. & Bazant, M. Z. Nonequilibrium Thermodynamics of Porous Electrodes. *J. Electrochem. Soc.* **159**, A1967–A1985 (2012).
25. Bai, P. & Tian, G. Statistical kinetics of phase-transforming nanoparticles in LiFePO<sub>4</sub> porous electrodes. *Electrochim. Acta* **89**, 644–651 (2013).
26. Levi, M. D. *et al.* Collective Phase Transition Dynamics in Microarray Composite Li<sub>x</sub>FePO<sub>4</sub> Electrodes Tracked by in Situ Electrochemical Quartz Crystal Admittance. *J. Phys. Chem. C* **117**, 15505–15514 (2013).

27. Bai, P. & Bazant, M. Z. Charge transfer kinetics at the solid-solid interface in porous electrodes. *Nature Commun.* **5**, 3585 (2014).
28. Newman, J. & Thomas-Alyea, K. E. *Electrochemical Systems*. (Prentice Hall, 2004).
29. Bazant, M. Z. Theory of Chemical Kinetics and Charge Transfer based on Nonequilibrium Thermodynamics. *Acc. Chem. Res.* **46**, 1144–1160 (2013).
30. Bluhm, H. *et al.* Soft X-ray microscopy and spectroscopy at the molecular environmental science beamline at the Advanced Light Source. *J. Electron Spectros. Relat. Phenomena* **150**, 86–104 (2006).
31. Kilcoyne, A. L. D. *et al.* Interferometer-controlled scanning transmission X-ray microscopes at the Advanced Light Source. *J. Synchrotron Radiat.* **10**, 125–136 (2003).
32. Kilcoyne, D. *et al.* A new Scanning Transmission X-ray Microscope at the ALS for operation up to 2500eV. in *10th Int. Conf. Synchrotron Radiat. Instrum.* 465–468 (2010).
33. Liu, X. *et al.* Phase Transformation and Lithiation Effect on Electronic Structure of  $\text{Li}_x\text{FePO}_4$ : An In-Depth Study by Soft X-ray and Simulations. *J. Am. Chem. Soc.* **134**, 13708–13715 (2012).
34. Cogswell, D. A. & Bazant, M. Z. Theory of Coherent Nucleation in Phase-Separating Nanoparticles. *Nano Lett.* **13**, 3036–3041 (2013).
35. Gibot, P. *et al.* Room-temperature single-phase Li insertion/extraction in nanoscale  $\text{Li}_x\text{FePO}_4$ . *Nature Mater.* **7**, 741–747 (2008).
36. Bai, P., Cogswell, D. A. & Bazant, M. Z. Suppression of Phase Separation in  $\text{LiFePO}_4$  Nanoparticles During Battery Discharge. *Nano Lett.* **11**, 4890–4896 (2011).
37. Malik, R., Zhou, F. & Ceder, G. Kinetics of non-equilibrium lithium incorporation in  $\text{LiFePO}_4$ . *Nature Mater.* **10**, 587–590 (2011).
38. Yu, X. *et al.* High rate delithiation behaviour of  $\text{LiFePO}_4$  studied by quick X-ray absorption spectroscopy. *Chem. Commun.* **48**, 11537–9 (2012).
39. Cahn, J. W. On Spinodal Decomposition. *Acta Metall.* **9**, 795–801 (1961).
40. Allen, S. M. & Cahn, J. W. A Microscopic Theory for Antiphase Boundary Motion and its Application to Antiphase Domain Coarsening. *Acta Metall.* **27**, 1085–1095 (1979).
41. Cogswell, D. A. & Bazant, M. Z. Coherency strain and the kinetics of phase separation in  $\text{LiFePO}_4$  nanoparticles. *ACS Nano* **6**, 2215–2225 (2012).

42. Morgan, D., Van der Ven, A. & Ceder, G. Li Conductivity in  $\text{Li}_x\text{MPO}_4$  (M = Mn, Fe, Co, Ni) Olivine Materials. *Electrochem. Solid-State Lett.* **7**, A30–A32 (2004).
43. Srinivasan, V. & Newman, J. Existence of Path-Dependence in the  $\text{LiFePO}_4$  Electrode. *Electrochem. Solid-State Lett.* **9**, A110–A114 (2006).
44. Orvananos, B., Ferguson, T. R., Yu, H.-C., Bazant, M. Z. & Thornton, K. Particle-Level Modeling of the Charge-Discharge Behavior of Nanoparticulate Phase-Separating Li-Ion Battery Electrodes. *J. Electrochem. Soc.* **161**, A535–A546 (2014).
45. Gaberscek, M., Kuzma, M. & Jamnik, J. Electrochemical kinetics of porous, carbon-decorated  $\text{LiFePO}_4$  cathodes: separation of wiring effects from solid state diffusion. *Phys. Chem. Chem. Phys.* **9**, 1815–1820 (2007).
46. Meethong, N., Huang, H.-Y. S., Speakman, S. A., Carter, W. C. & Chiang, Y.-M. Strain Accommodation during Phase Transformations in Olivine-Based Cathodes as a Materials Selection Criterion for High-Power Rechargeable Batteries. *Adv. Funct. Mater.* **17**, 1115–1123 (2007).
47. Omenya, F. *et al.* Why Substitution Enhances the Reactivity of  $\text{LiFePO}_4$ . *Chem. Mater.* **25**, 85–89 (2013).
48. Ravnsbæk, D. B. *et al.* Extended Solid Solutions and Coherent Transformations in Nanoscale Olivine Cathodes. *Nano Lett.* **14**, 1484–91 (2014).
49. Kang, B. & Ceder, G. Battery materials for ultrafast charging and discharging. *Nature* **458**, 190–3 (2009).
50. Park, K. *et al.* Enhanced Charge-Transfer Kinetics by Anion Surface Modification of  $\text{LiFePO}_4$ . *Chem. Mater.* **24**, 3212–3218 (2012).

## **Acknowledgements**

The research at Stanford was supported by Samsung Advanced Institute of Technology Global Research Outreach program, and by startup funding from Stanford School of Engineering and Precourt Institute for Energy. Support for the research at MIT was provided by the Samsung-MIT Program for Materials Design in Energy Applications. The research at Sandia was supported by U.S. Department of Energy through the Sandia Laboratory Directed research and Development program under Contract DE-AC04-94AL85000. The Advanced Light Source is supported by the Director, Office of Science, Office of Basic Energy Sciences, of the U.S. Department of Energy under Contract No. DE-AC02-05CH11231. Beam line 5.3.2.1 at the Advanced Light Source was funded through a donation by the King Abdullah University of Science and Technology. Y. L. was supported by the National Science Foundation Graduate Research Fellowship under Grant No. DGE-114747. We acknowledge Mark Homer of Sandia and John Perrino of Stanford for ultramicrotoming. We thank Johanna Nelson Weker of the Stanford Synchrotron Radiation Lightsource for insightful discussions.

## **Author Contributions**

Y. L., F. E. G., and W. C. C. conceived the experiments. K. F. and F. E. G. prepared the LFP samples for imaging. Y. L., T. T., and A. L. D. K. performed the SoC imaging. J. D. S. and Y. L. performed the TEM imaging. Y. L. analysed the active particle population from the images. T. F., R. B. S., and D. A. C. conceived and created the phase-field model. W. C. C. and M. Z. B. supervised the project. All authors participated in writing the manuscript.

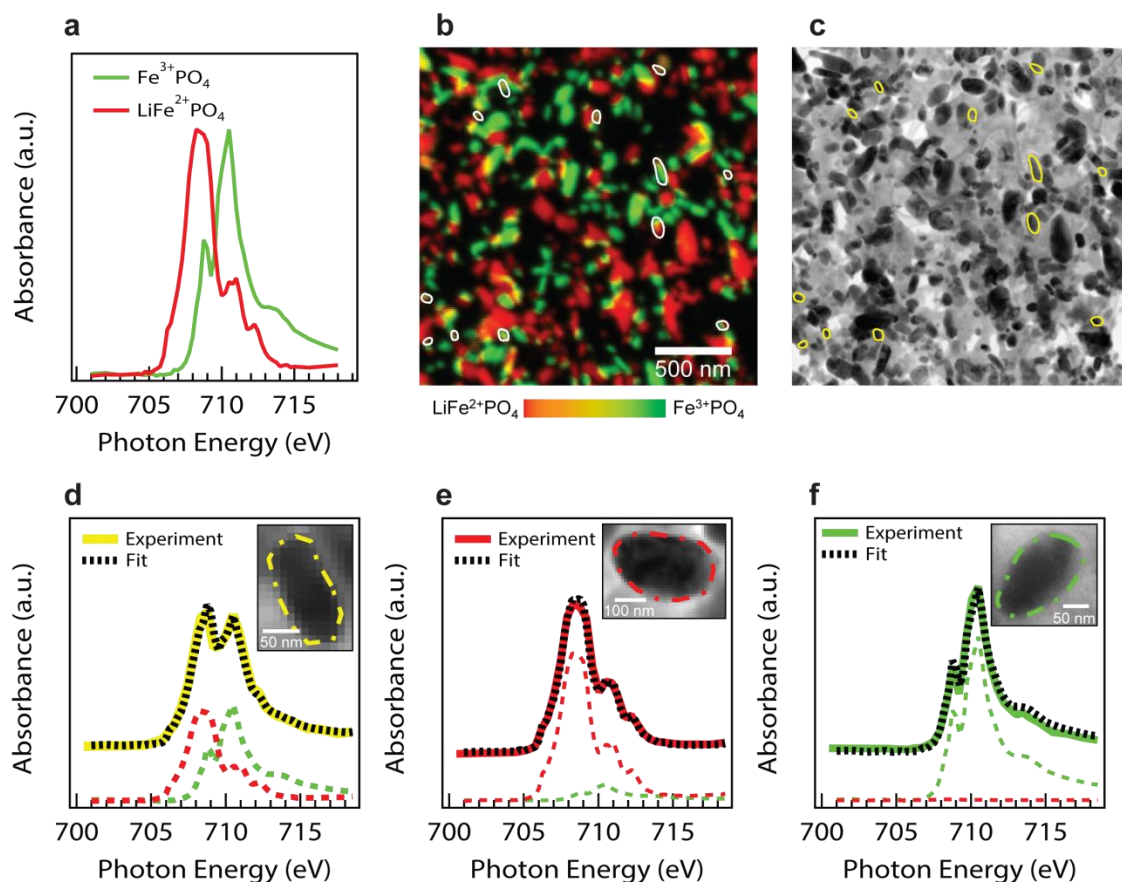


**Fig. 1: Lithium fraction within each particle of an electrode charged at 5.0 C to 50% SoC.**

(a) Reference X-ray absorption spectra for fully lithiated and delithiated particles. The state-of-charge map in (b) was produced by fitting a linear combination of the references to every single-pixel spectra. The hue represents lithium fraction, and the brightness designates the particle thickness. We used the TEM image of the same electrode regions (c), which also includes faint features of carbon black and the binder, to identify the boundary of each particle. We outline actively-intercalating particles in (b) and (c). (d)-(f) show typical particles and their absorption spectra.

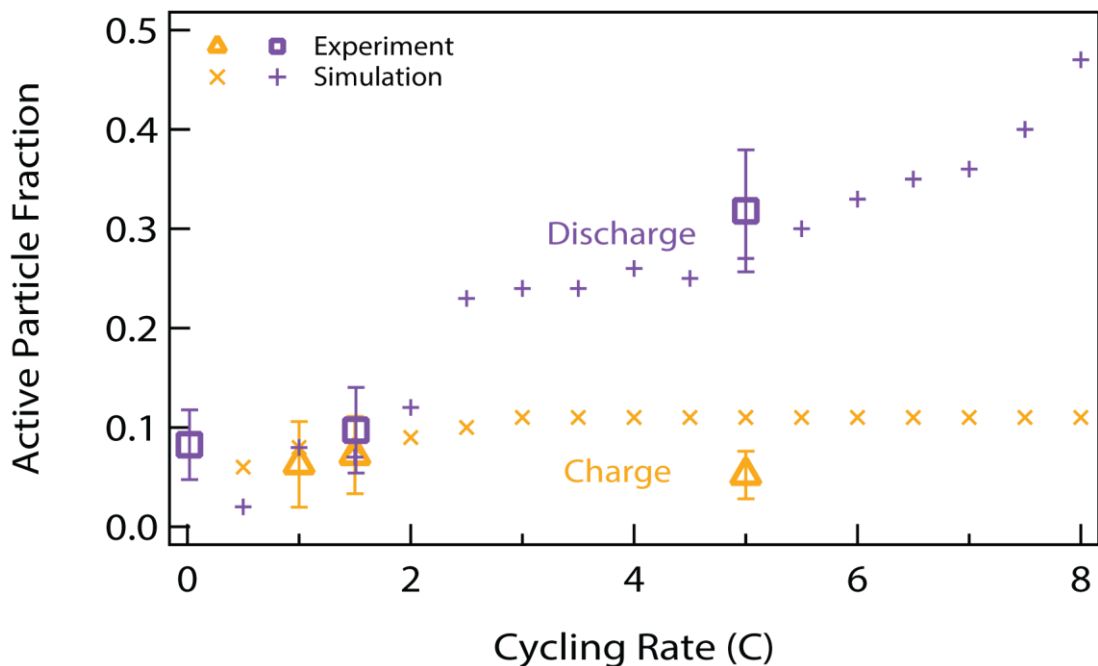


**Fig. 2: Active particle fraction as a function of cycling condition.** The fraction of actively-intercalating particles varies as a function of rate in both the experiments and the phase-field simulations. The experimental error bars are calculated assuming a binomial distribution (active or not active) taken at three standard deviations. We reanalysed data from our previous work for the 1.0 C charge experiment<sup>16</sup>.



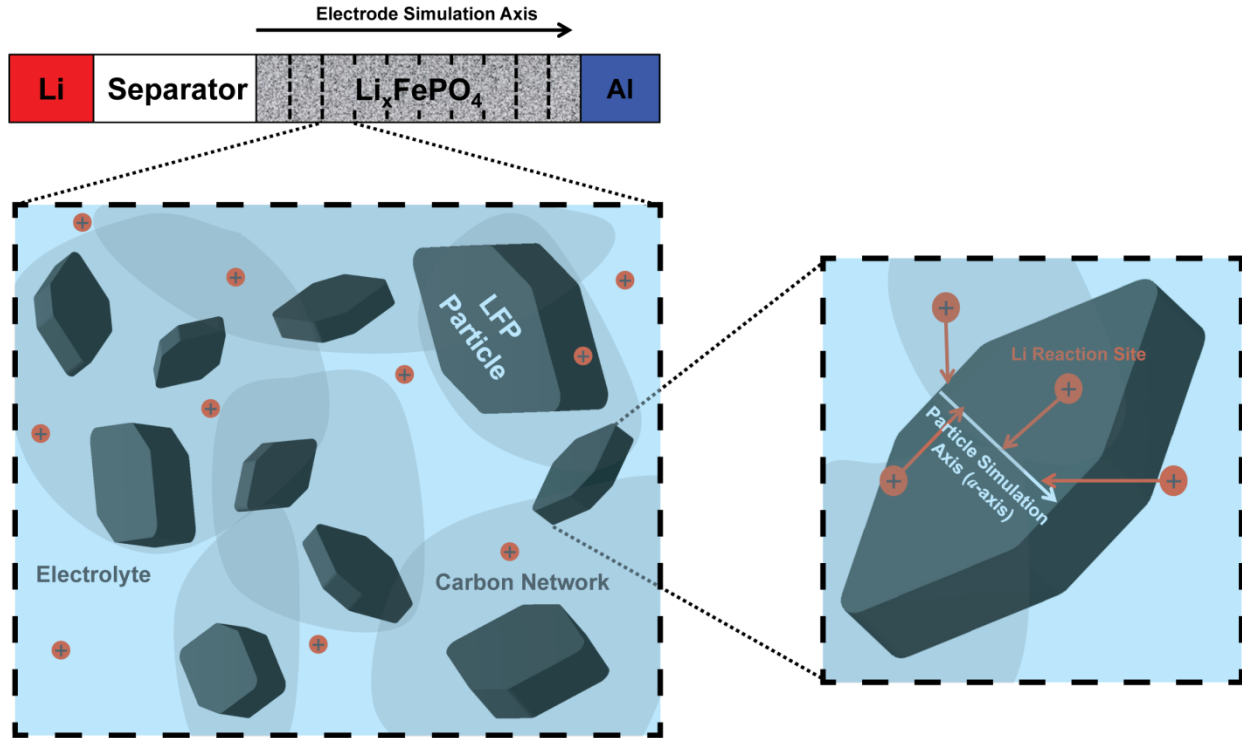


**Fig. 3: Schematic of the combined porous electrode and phase-field model.** We divide the LFP electrode into 10 representative volumes, each containing 10 LFP particles immersed in a liquid electrolyte and connected electronically through the carbon network. A one-dimensional Cahn-Hilliard equation (Eq. 2) governs the Li diffusional chemical potential along the *a*-axis of each particle. A Butler-Volmer equation (Eq. 3) governs the insertion and removal of Li.

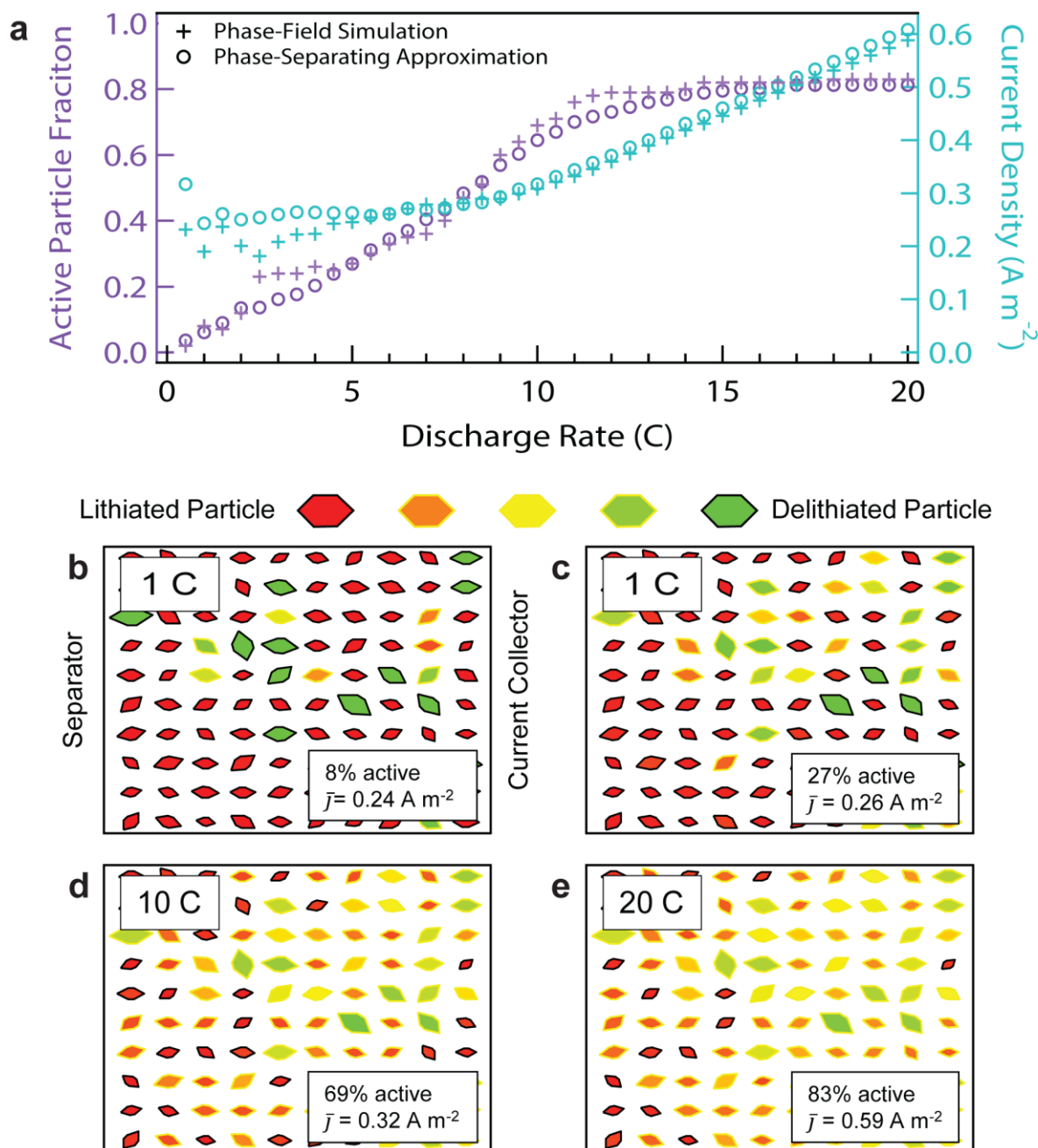


**Fig. 4: Results from combined phase-field and porous electrode simulations of LFP.** (a) plots the active particle fraction and current density as a function of discharge rate at a 50% SoC. Simulation results using a phase-separating approximation are also shown. For all rates less than  $I_{\text{crit}}$ , higher current increases the number of active particles, but the average current density for

the active particles remains approximately constant with discharge rate. Once the active particle fraction saturates, the current density increases in regime 2. (b)-(e) show simulation snapshots of 50% discharged electrodes at different rates; the hue represents the lithiation fraction in the snapshots. A preferential lithiation of the small particles result in a larger number of lithiated (red) particles in the simulation; due to wiring, such preferential lithiation of small particles is not observed experimentally (Fig. S13). To show smaller particles in this figure, the length of the particles in the schematic is proportional to the square root of the experimentally-measured particle length (Fig. S1).

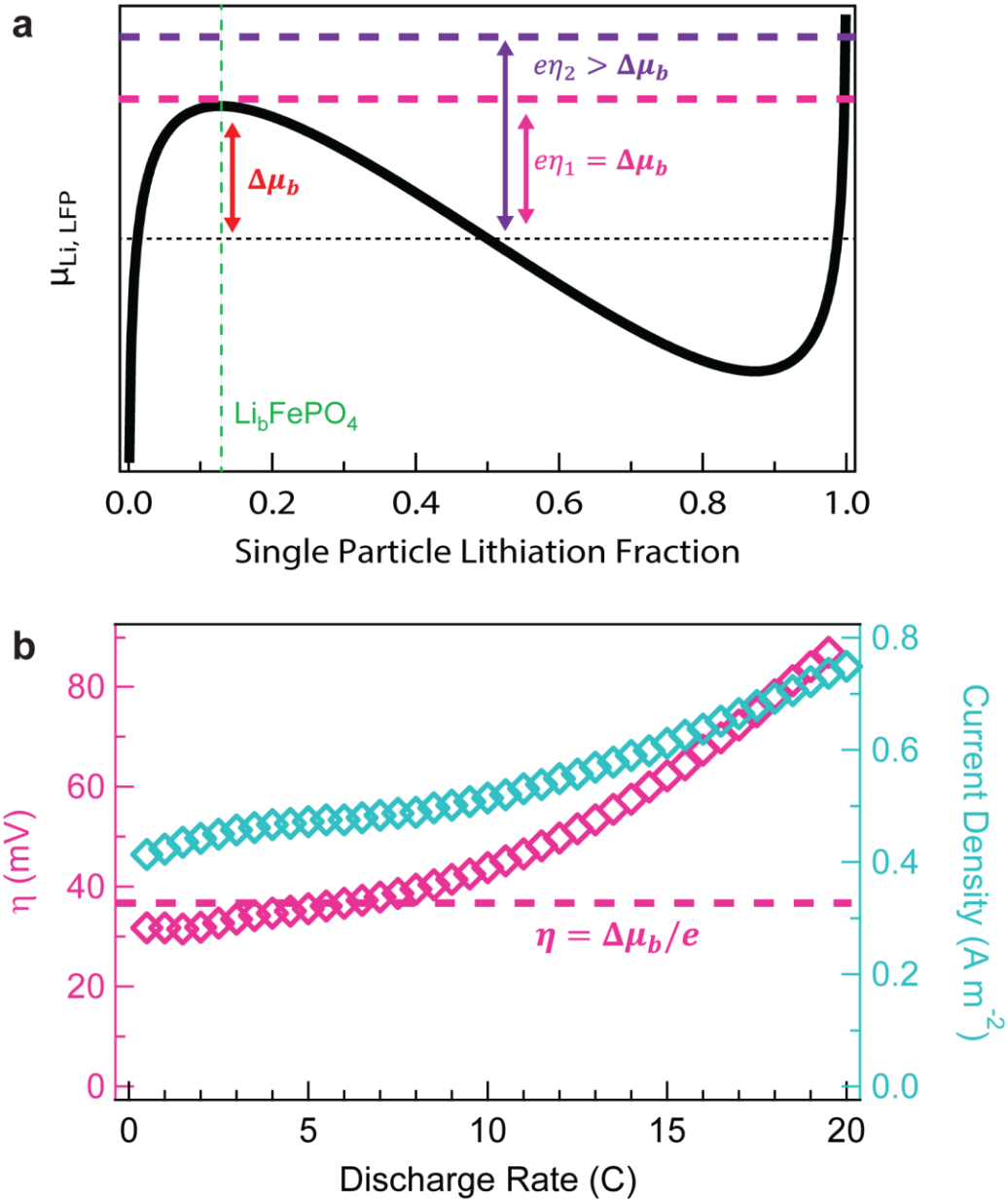


**Fig. 5: Simulated behaviour of a typical LFP particle.** (a) shows the diffusional chemical potential of Li as a function of the particle's lithiation fraction.  $\mu_{Li,LFP}$  contains a transformation barrier ( $\Delta\mu_b$ ), defined as the difference between the local maxima and the diffusional chemical potential at the centre of the miscibility gap. (b) plots the particle's reaction overpotential and current density as a function of discharge rate when the particle's SoC is 50%. Because we

assume solid-state diffusion to be fast, the reaction overpotential is entirely consumed by the surface reaction through Eq. 3. In regime 1, the electrode ensemble potential is approximately equal to the top of the transformation barrier because not all particles are active, so the reaction overpotential  $\eta_1$  for active particles is approximately equal to  $\Delta\mu_b/e$ . In regime 2, the reaction overpotential  $\eta_2$  is above  $\Delta\mu_b/e$ , so all particles lithiate concurrently. The reaction overpotential and current density of the particle increase with discharge rate to accommodate the extra current. We note that the current density here is somewhat higher than in Fig. 4a because one typical particle is considered, whereas in Fig. 4a the current density is averaged over all active particles.

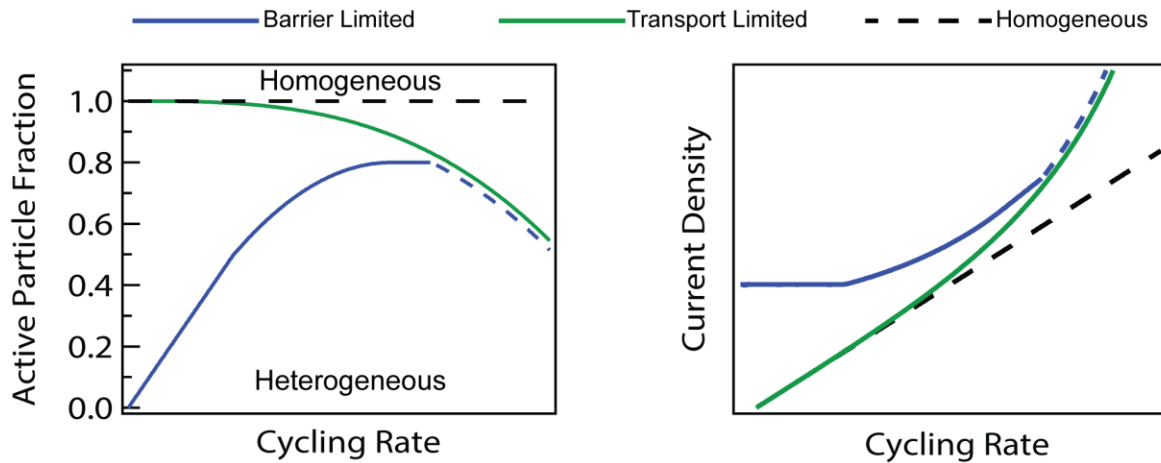


**Fig. 6: Schematic representation of the proposed transformation-barrier-limited model against prevailing models.** A homogeneous electrode assumes that the current is distributed evenly to all particles, so the current density increases uniformly with cycling rate. An electrode-transport-limited model results in an electrode-level moving front<sup>24</sup> and reduced active particle population at high rates, but the current distribution is homogeneous at lower rates. In our transformation-barrier-limited model, the active particle population is small at low rates, indicating a low degree of current homogeneity. At higher rates, the current homogeneity increases, but electrode transport likely limits the active particle population at very high rates (dashed blue lines).

**Current-Induced Transition from Particle-by-Particle to Concurrent Intercalation in  
Phase-Separating Battery Electrodes**

**Supplementary Information**

Yiyang Li, Farid El Gabaly, Todd R. Ferguson, Raymond B. Smith, Norman C. Bartelt,

Joshua D. Sugar, Kyle R. Fenton, Daniel A. Cogswell, A. L. David Kilcoyne,

Tolek Tyliczszak, Martin Z. Bazant, William C. Chueh \*

\*Corresponding Author: Email: [wchueh@stanford.edu](mailto:wchueh@stanford.edu)

## 1. Battery Powder Particle Size Distribution and Electrochemical Cycling

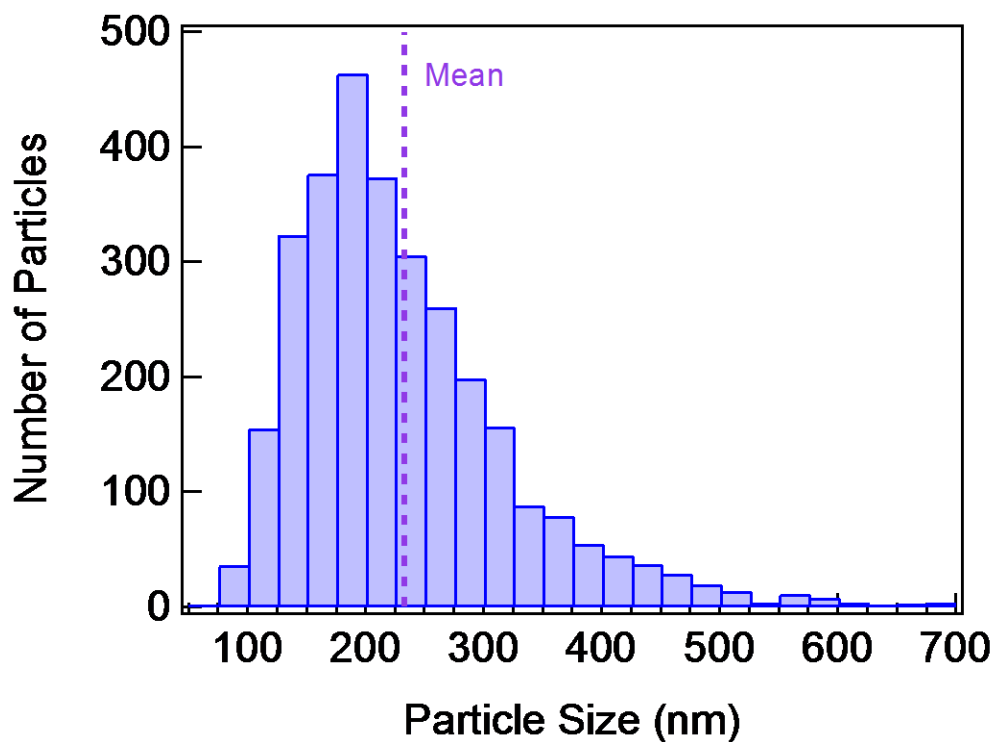


**Fig. S1: Lithium iron phosphate (LFP) particle size distribution.** The particle size, determined from the transmission electron micrographs, is defined as the length of the longest distance between any two points in the particle that passes through the particle's centre of gravity. This histogram includes all LFP particles analysed in this work.



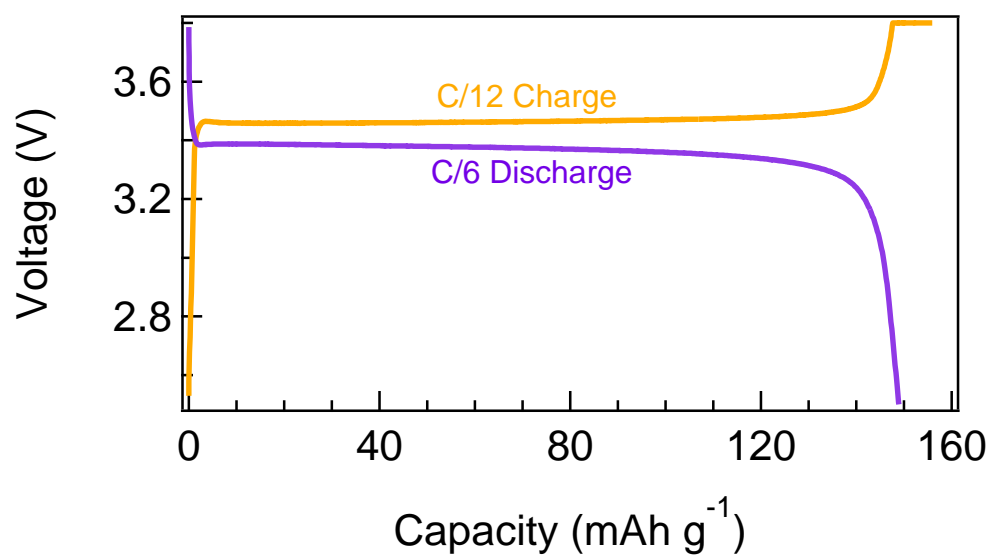


**Fig. S2: Typical charge and discharge curves.**

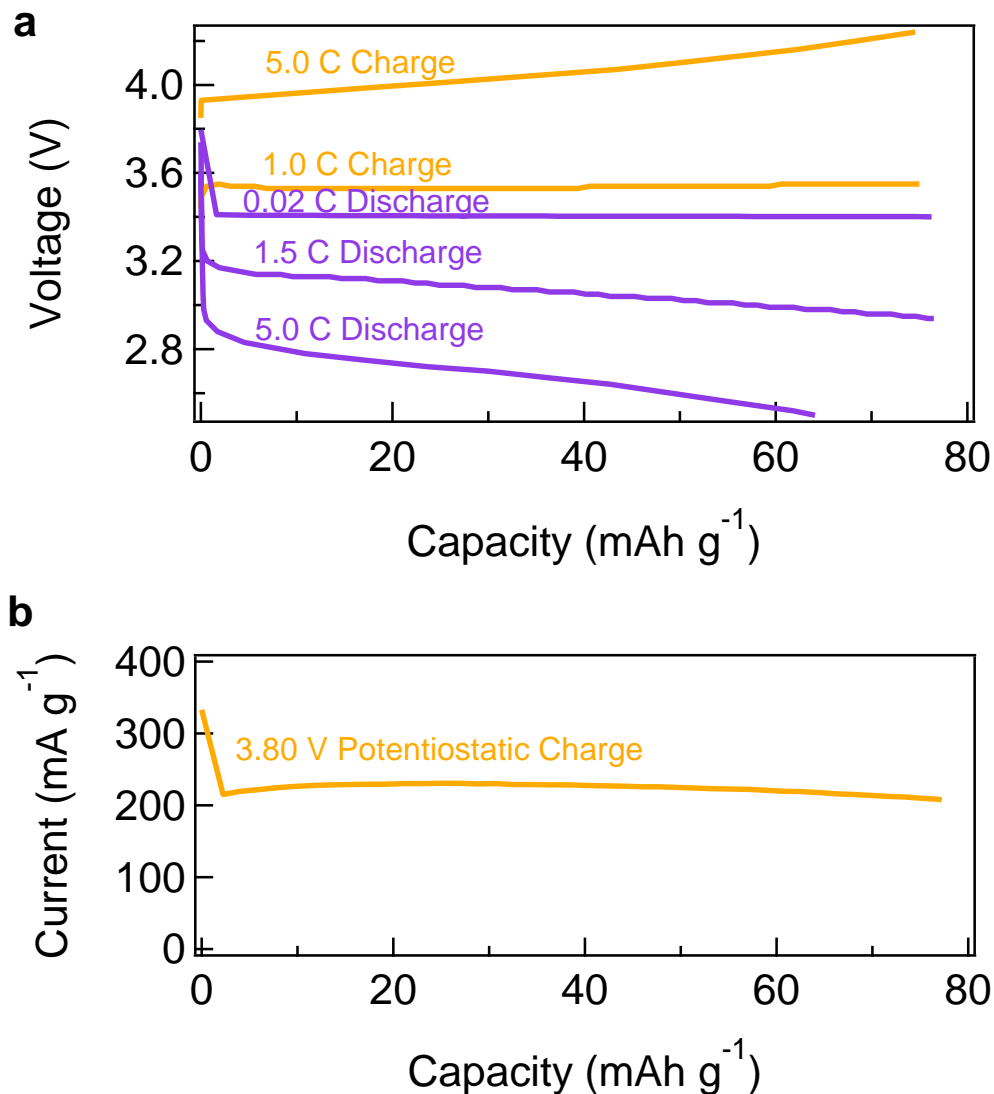


**Fig. S3 Electrochemical preparation of the LFP electrodes imaged by X-ray microscopy.** (a) The 5.0 C charge, 1.0 C charge, 0.02 C discharge, 1.5 C discharge, and 5.0 C discharge electrodes were prepared under constant current conditions. (b) The 1.5 C charge electrode was prepared under potentiostatic conditions at 3.8 V. Because the current is approximately constant past 5 mAh g<sup>-1</sup>, the result is comparable to the galvanostatically-cycled samples.

## 2. X-ray Microscopy and Analysis

### *LiFePO<sub>4</sub> and FePO<sub>4</sub> references*

After five formation cycles, we cycled lithium iron phosphate (LFP) electrodes at C/50 to 3.8 V or 2.5 V to generate charged (Fe<sup>3+</sup>PO<sub>4</sub>) and discharged (LiFe<sup>2+</sup>PO<sub>4</sub>) reference samples. After cycling, we disassembled the references and loaded some of the powder onto Si<sub>3</sub>N<sub>4</sub> windows. We raster-scanned  $\sim 2 \times 2$   $\mu\text{m}$  regions while varying the X-ray photon energy across the Fe L<sub>3</sub> absorption edge, and averaged the single-pixel spectrum to yield the fully charged and discharged reference spectra (Fig. 1a).

### *State-of-Charge Maps*

To obtain state-of-charge (SoC) maps, we raster-scanned several  $5 \times 5$   $\mu\text{m}$  regions in each electrode. At each region, we obtained about 28 images, each at a different photon energy, across the Fe L<sub>3</sub> absorption edge. Post-processing was carried using Axis2000<sup>1</sup>. After aligning the images acquired at different photon energies, we converted transmission images to optical density images.

We fitted a linear combination of the LiFe<sup>2+</sup>PO<sub>4</sub> and Fe<sup>3+</sup>PO<sub>4</sub> reference spectra to the optical density at each pixel. The results were used to generate the SoC maps. The pixel brightness is given by the total optical density (i.e., thickness of the sample), whereas the hue represents the fraction of LiFePO<sub>4</sub> and FePO<sub>4</sub>. A red hue is assigned to the pure LiFePO<sub>4</sub> state (0% SoC), and a green hue is assigned to the pure FePO<sub>4</sub> state (100% SoC). To confirm the robustness of the reference samples, we generated state-of-charge (SoC) maps for electrochemically-cycled FePO<sub>4</sub> and LiFePO<sub>4</sub> (Fig. S5), which show that they are fully charged and discharged, respectively.

### *Average State-of-Charge*

We calculated the average SoC of each region by averaging the single-pixel SoC weighed by the thickness (Fig. S6). On charging, regions closer to the separator have a slightly higher SoC; on discharging, regions closer to the separator have a slightly lower SoC. In both cases the dependence is weak. This implies that ionic transport across the thickness of the electrode is slightly slower than electronic transport. At low rates, the average SoC matches the electrochemically-determined values well. At higher rates, however, some deviations are observed. We attribute this to heterogeneity electronic and ionic wiring in the porous electrode, which would result in certain regions being more charged or discharged than others.

### *Single-particle State-of-Charge*

To carry out single-particle SoC analysis, we first traced well-isolated particles in the transmission electron micrographs. Typically, we identified between 120 and 200 particles in each  $5 \times 5 \mu\text{m}$  region. Next, we correlated each particle in the transmission electron micrograph to the corresponding particle in the SoC map. Particles with a SoC between 20% and 80% are identified as actively intercalating (see main text for detailed discussions). Figures 1b-c and S4 highlights the active particles for an imaged region in each electrode.

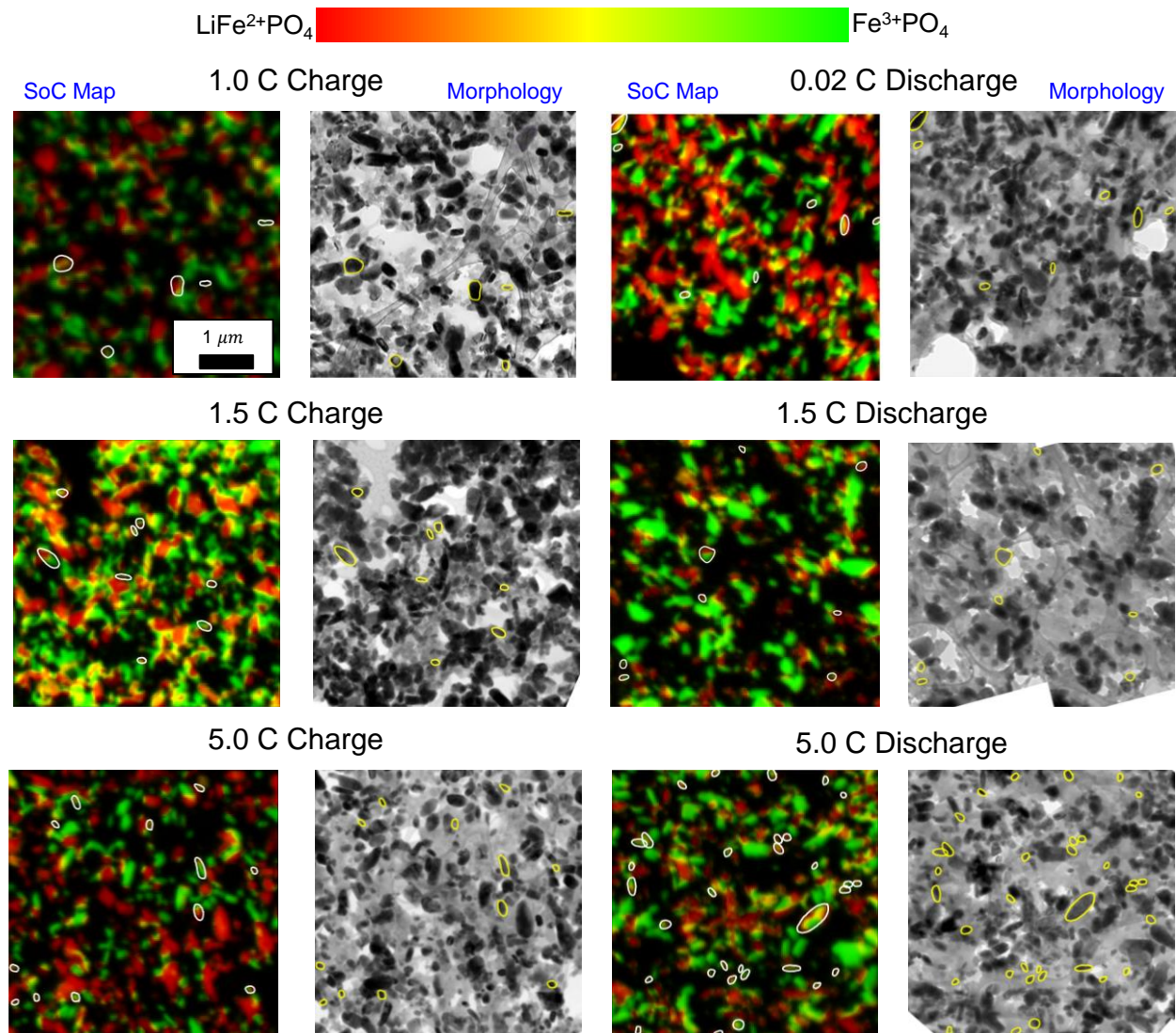


**Fig. S4: SoC map and corresponding TEM**

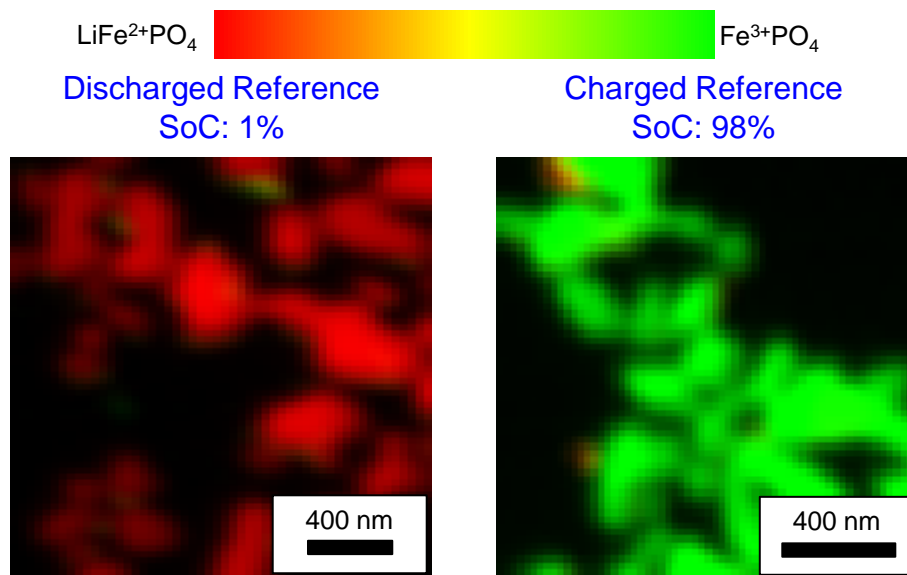


**Fig. S5: SoC maps for LiFePO<sub>4</sub> and FePO<sub>4</sub>**

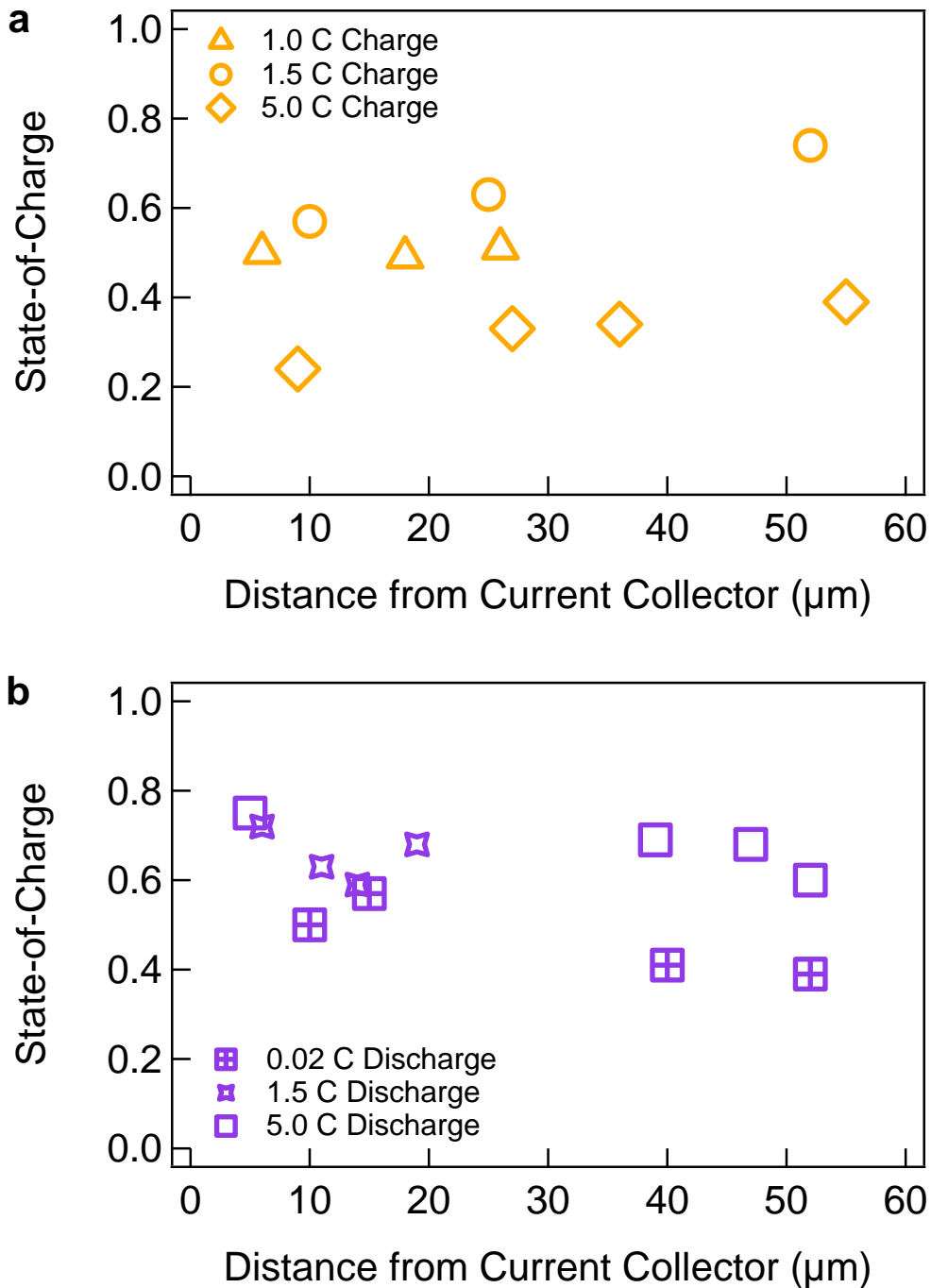


**Fig. S6: State-of-Charge as a function of position in the LFP electrode for (a) charging and (b) discharging electrodes. The absence of a strong (de)lithiation front shows that electrolyte transport in the porous electrode is fast.**

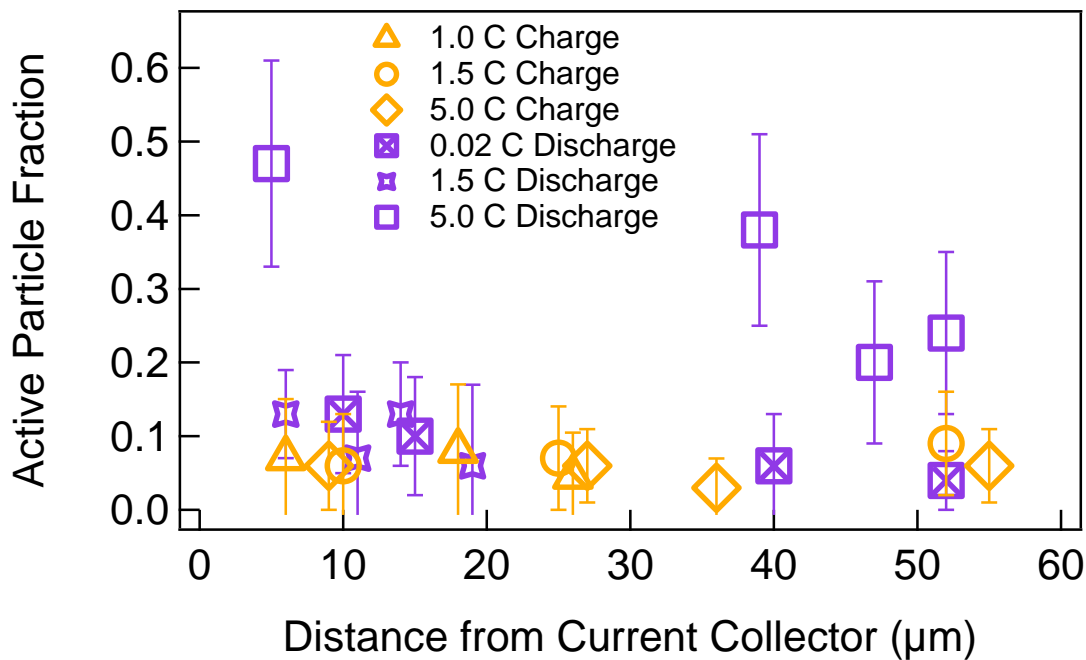


**Fig. S7: Position dependence of the active particle fraction in the electrode.** The active particle fraction does not significantly vary with position. All LFP electrodes are 60  $\mu\text{m}$  thick from the current collector to the separator, except for the 1.0 C electrode, which is 35  $\mu\text{m}$  thick. The error bars are calculated assuming a binomial distribution (active or not active) taken at three standard deviations.



### 3. Sensitivity Analysis

We performed two sensitivity analyses on our quantification protocol. We first evaluated the sensitivity of the actively-intercalating population to the particle selection method. In the first method (which we adopted in this work), we considered only well-isolated particles thicker than  $\sim 40$  nm. In the second method, we considered thin particles as well as moderately overlapped particles. Figure S8 shows the actively-intercalating particle population determined using these two quantification methods. The active particle fraction is nearly independent of the particle selection protocol.

Next, we evaluated the sensitivity of the active population to the threshold of actively-intercalating particles. Specifically, we compared using a (1) 20-80% SoC and (2) 10-90% SoC definition for active particles (Fig. S9). The active particle fraction is higher for the 10-90% threshold than the 20-80% threshold. This is expected as some Li-rich and Li-poor particles may have been misidentified as active due to insufficient signal-to-noise when using 10-90% threshold. However, the qualitative trends (rate dependence and asymmetry between charge and discharge) remain independent of the quantification protocol.

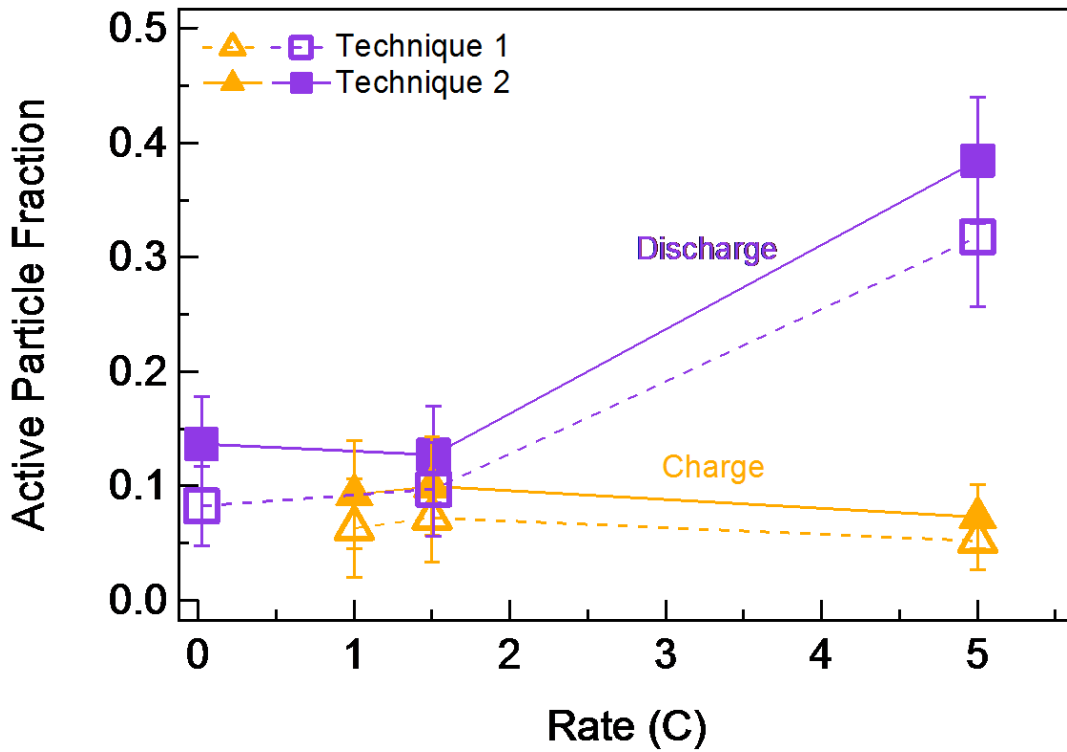


**Fig. S8: Sensitivity of the active population to the particle selection method.** The two methods here differ in the definition of a particle, but yield similar results (see main text for details). The error bars equal three standard deviations assuming the particles follow a binomial state (active or not active).

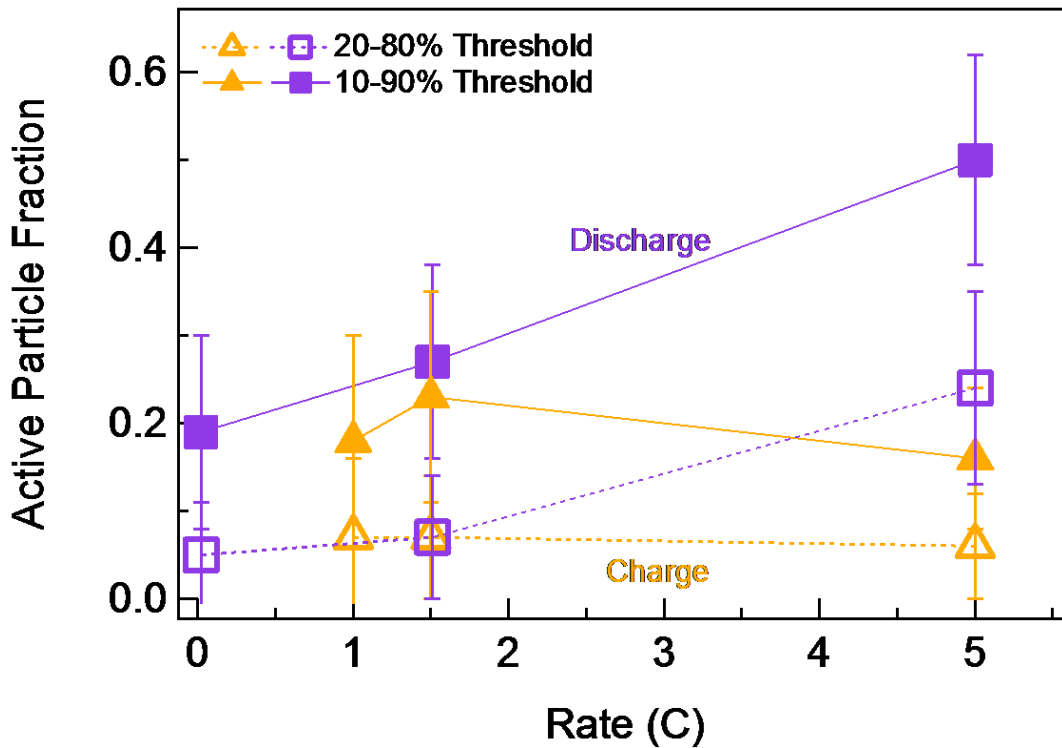


**Fig. S9: Sensitivity of the active population to the active particle definition.** The first technique defines a particle between 20-80% SoC as an active particle. The second technique defines it as between 10-90% SoC. While the active particle fraction is higher with the 10-90% threshold, the qualitative trends (rate dependence and asymmetry between charge and discharge) remain independent of the quantification method. The error bars equal three standard deviations assuming the particles obey a binomial state (active or not active). One region in each electrode was analysed, thus giving different active particle fractions and larger error bars than those plotted in Figs 2 and S8, which included all imaged regions.

#### 4. Carbon Loading Variation

To confirm that most of the voltage results from Ohmic losses in the porous electrode, we compared the voltage of coin cells with 5 wt% and 20 wt% carbon loading. The electrodes consist of 74 wt% or 89 wt% carbon-coated lithium iron phosphate (LFP), 5 wt% or 20 wt% acetylene black (Alfa Aesar 45527), and 6 wt% polyvinylidene fluoride (PVDF). PVDF was dissolved in N-methyl-2-pyrrolidone (NMP); LFP and acetylene black were added to the slurry and stirred for ~ 18 h at 1,000 rpm. The NMP: solid ratio was 3.5:1.0 (wt/wt) for the 20% wt carbon slurry and 2.75:1.0 (wt/wt) for the 5% wt carbon slurry. The slurry was then cast onto a 15- $\mu\text{m}$  aluminum current collector using a doctor blade. Solvent was removed at ~ 50° C and dried under vacuum at 90° C for 24 h. The electrode mass loading and thickness were ~ 3 mg cm<sup>-2</sup> and ~ 15  $\mu\text{m}$ , respectively. The electrodes were assembled into 2016 coin cells using two 25  $\mu\text{m}$  Celgard separators and a Li anode immersed in a 1M LiPF<sub>6</sub> electrolyte in 4:3:3 (vol/vol/vol) ethylene carbonate: dimethyl carbonate: diethyl carbonate electrolyte.

The electrodes underwent two or five formation cycles at between C/8 and C/10 charge and between C/4 and C/5 discharge, with cutoff voltages at 3.8 and 2.5 V, respectively. The average discharge capacity of the batteries was 152 mAh g<sup>-1</sup> with a standard deviation of 4 mAh g<sup>-1</sup>. The capacity obtained from the formation cycle was independent of carbon loading. Figure S10 shows the voltage as a function of charging and discharged rates when the electrodes were cycled partially between fully (dis)charged and 50 mAh g<sup>-1</sup>.

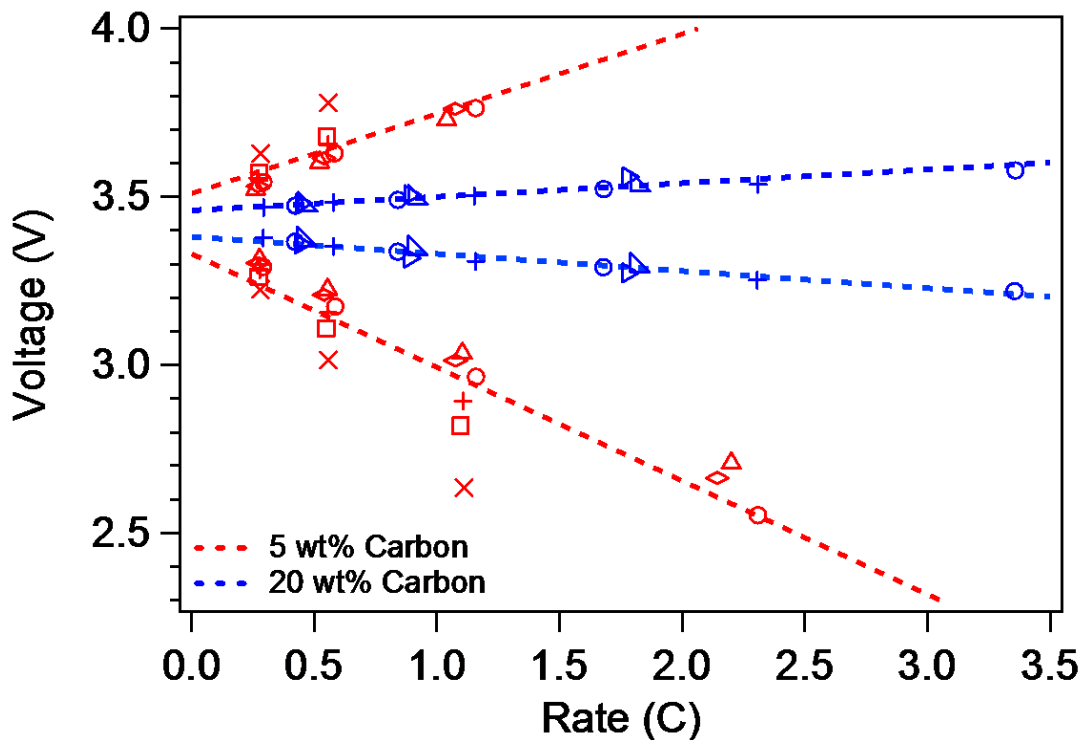


**Fig. S10: Rate-dependent voltage of LFP electrodes at different carbon loadings at 33% state-of-(dis)charge.** The dashed lines are linear fits of the voltage as a function of rate. The electrodes were cycled partially between fully (dis)charged and  $50 \text{ mAh g}^{-1}$ . Some voltages are unavailable at higher rates because the battery reached the cutoff voltage of 3.8 V or 2.5 V before (dis)charging  $50 \text{ mAh g}^{-1}$ . Each symbol represents a different battery made from the same electrode sheet.

## 5. Numerical Porous Electrode Simulations

The simulations were conducted using a modified porous electrode model similar to the one developed by Ferguson and Bazant<sup>3</sup>. The LFP solid particles were modelled with a phase-field approach. A reaction model couples the solid phase with ion transport in the electrolyte. Supplemental ref. 3 provides a detailed derivation of the model. Given the relatively small average particle size in our experiment, we assume lithium intercalation in LFP particles to be reaction limited (i.e., no solid-state diffusional gradient along the fast  $b$ -axis along the solid). We simulated the lithium diffusional chemical potential and current in two dimensions using finite volume discretization: along the  $a$ -axis of individual particles, and along the thickness of the electrode spanning the porous electrode sandwiched between the current collector and the separator (Fig. 3). The reaction at the lithium anode is assumed to be fast.

We simultaneously solved for the lithium distribution within 100 representative particles inside the porous electrode. We divided the positive electrode into ten evenly spaced representative volumes; each volume contains ten particles of different sizes.

### *Particle Shape*

We simulated plate-like particles inspired by those from Supplementary ref. 4 and 5, with a schematic shown in Fig. 3. We randomly selected 100 particles (10 particles in each solid volume, with 10 different solid volumes at different positions in the electrode) from our experimental particle size distribution (Fig. S1). In the absence of orientation information from our transmission electron micrographs, we made the following assumptions about the particle sizes. We designate the  $c$ -axis to equal the values plotted in Fig. S1. The ratio between the  $a$ -axis and  $c$ -axis is taken to equal 1:1.92. We assume the  $b$ -axis thickness equals  $\sqrt{A_{ac}}/2$ , where

$A_{ac}$  equals the area of the  $ac$  surface. While we chose this specific model particle, our results are not sensitive to the actual particle size and morphology.

### *Transport in Electrolyte*

The electrolyte occupies the space in the pores of each representative electrode volume with volume fraction  $\epsilon$ . Combined, the particles represent a total active volume in the electrode,  $(1 - \epsilon)P_L$ , where  $P_L$  is the active material loading percent by volume. Cation and anion fluxes in the binary electrolyte are governed by the Nernst-Planck equation:

$$N_{\pm} = -D_{chem,\pm}\epsilon\nabla c_{\pm,yte} - \frac{ez_{\pm}}{k_bT}D_{\pm}\epsilon c_{\pm,yte}\nabla\phi \quad (1)$$

where the subscript “+” and “-” denote the cation and anion, respectively,  $c_{yte}$  is the concentration of lithium in the electrolyte,  $z$  is the formal charge of the ion,  $e$  is the elementary charge,  $\phi$  is the electrostatic potential,  $k_b$  is Boltzmann’s constant, and  $T$  is the temperature (room temperature in the simulations).  $D_{chem,\pm}$  are the chemical diffusivities of the cations and anions in the electrolyte, and  $D_{\pm}$  are the dilute limit diffusivities. Applying mass conservation and electroneutrality yields:

$$\epsilon\frac{\partial c_{yte}}{\partial t} + R_V = \nabla \cdot (\epsilon D_{amb}\nabla c_{yte}) - \nabla \cdot \left(\frac{t_+\mathbf{i}}{e}\right) \quad (2)$$

where  $D_{amb} \equiv \frac{z_+D_+D_{chem,-} + z_-D_-D_{chem,+}}{z_+D_+ + z_-D_-}$  is an ambipolar diffusivity of the electrolyte,

$t_+ \equiv \frac{z_+D_+}{z_+D_+ + z_-D_-}$  is the cation transference number, and  $\mathbf{i} = ez_+N_+ - ez_-N_-$  is the electrical current density in the electrolyte. Based on electroneutrality,  $c_{yte} = z_+c_{+,yte} = z_-c_{-,yte}$ .  $R_V$  is the total reaction rate summed over the particles in a solid volume of the electrode ( $V$ ) at a

given position along the thickness of the electrode, which we relate to the electrolyte current density via charge conservation:

$$R_V = (1 - \epsilon)P_L \sum_p \frac{V_p}{V_u} \frac{\partial \bar{c}_s}{\partial t} = -\nabla \cdot \left( \frac{\mathbf{i}}{e} \right) \quad (3)$$

where  $p$  indexes particles in a volume,  $V_p$  is the volume of particle  $p$ ,  $V_u$  is the total volume of all particles in the solid volume, and  $\bar{c}_s$  is the average concentration of lithium in particle  $p$ . This volumetric reaction rate is the first significant modification to the work in Supplementary ref. 3. Whereas Ferguson and Bazant<sup>3</sup> simulated a single representative particle per volume, here we picked a distribution of particles in each volume, and the volumetric reaction rate is thus modified accordingly.

The total current is constrained in our constant current simulations by integrating the reaction rates over the entire positive electrode:

$$\frac{I}{e} = \int_V R_V dV \quad (4)$$

We hold the total current constant by adjusting the applied voltage between the positive and negative current collectors. At the positive electrode current collector, we imposed a zero-flux boundary condition. We assume no overpotential at the Li anode as a result of fast reaction. We set the electrolyte concentration gradient at the anode to equal the value required by the overall current constraint and the cross-sectional area of the cell,  $A_{cell}$ :

$$-D_{amb} \nabla c_{yte} \Big|_{anode} = \frac{I}{eA_{cell}} \quad (5)$$



## Particle Reaction Rate

Using a one-dimensional phase-field model, we solved the reaction-limited Allen-Cahn-type equation to obtain the reaction rate in each particle. This solution to a one-dimensional particle has been shown to be comparable to a complete two-dimensional solution<sup>6</sup>. To reduce computational time, we discretized particles into 2 nm slices along the  $a$ -axis. While a 2 nm discretization along the  $a$ -axis is larger than the phase boundary<sup>7</sup>, our simulations showed no differences between a 1 nm and a 2 nm discretization. The reaction rate couples the transport of lithium in the electrolyte with the solid electrode particles. The reaction rate per area for the each particle in a single-electron process is given by a modified Butler-Volmer equation<sup>3,7</sup>

$$J = k_0 \frac{a_{Li,yte}^{1-\alpha} a_{Li,s}^{\alpha}}{\gamma_{TS}} \left[ \exp\left(-\frac{\alpha e \eta}{k_B T}\right) - \exp\left(\frac{(1-\alpha) e \eta}{k_B T}\right) \right] \quad (6)$$

where  $k_0$  is the rate constant,  $\alpha$  describes the phenomenological asymmetry, and  $a_{Li,s}$  and  $a_{Li,yte}$  are the activities of lithium in the solid particles (reduced state) and in the electrolyte (oxidized state), respectively.  $\gamma_{TS} = (1 - \tilde{c}_s)^{-1}$  is the activity coefficient of the transition state representing excluded sites in the transition state, and  $\tilde{c}_s$  is the reduced lithium concentration along the  $a$ -axis of the solid normalized to the number of Li sites. Here, we neglect departures from Butler-Volmer kinetics that has recently been observed in LFP<sup>8</sup>. The reaction overpotential is expressed as

$$\eta = \Delta \phi - \Delta \phi^{eq} \quad (7)$$

where  $\Delta \phi$  is the electrostatic potential difference between the metallic electron-conducting phase (i.e., carbon, which we assume for now to be a perfect conductor) and the electrolyte at the

particle. The second term,  $\Delta \phi^{eq}$ , represents the potential difference at equilibrium and relates to activities via the Nernst Equation:

$$\Delta \phi^{eq} = V^0 - \frac{k_B T}{e} \ln \left( \frac{a_{Li,s}^{eq}}{a_{Li,yte}^{eq}} \right) \approx V^0 - \frac{\mu_{Li,LFP}^{eq}}{e} + \frac{k_B T}{e} \ln \frac{c_{yte}^{eq}}{c_0} \quad (8)$$

where  $V^0$  is the standard potential,  $c_0$  is the initial electrolyte concentration,  $\mu_{Li,LFP}$  is the diffusional chemical potential of Li in an LFP particle (which varies along the  $a$ -axis of the LFP particles). The reaction rate is related to the solid phase concentrations by

$$\frac{\partial c_s}{\partial t} = \frac{A_p J}{V_p e}$$

where  $c_s$  is the concentration of lithium in the particle slice,  $A_p$  is the surface area of the particle.

From Supplementary ref. 3, we modelled the Li diffusional chemical potential in LFP as:

$$\mu_{Li,LFP} = \Omega_a (1 - 2\tilde{c}_s) + k_B T \ln \left( \frac{\tilde{c}_s}{1 - \tilde{c}_s} \right) - \frac{\kappa}{\rho_s} \nabla^2 \tilde{c}_s + \frac{B_0}{\rho_s} (\tilde{c}_s - \bar{c}_s) \quad (9)$$

where  $\Omega_a$  is the regular solution parameter,  $\kappa$  is the gradient penalty from the Cahn-Hilliard equation,  $B_0$  is the coherent stress penalty,  $\bar{c}_s$  is the average filling fraction of the particle, and  $\rho_s$  is the lithium site concentration. We accounted for lithium surface wetting discussed by Supplementary ref. 4 by imposing  $\tilde{c}_s = 0.98$  at the boundaries of each particle. This surface wetting, along with a size distribution within each simulated volume, is the other significant change to the model used in Supplementary ref. 3.

### *Barrier Height Variation*

Using the modified porous electrode model, we varied the barrier height by tuning the regular solution parameter  $\Omega_a$  to simulate materials with different transformation barriers. Figure

S11 plots the current density and active particle population for different barrier heights. The barrier for LFP has been shown to be around 40 meV<sup>4</sup>. This confirms that our qualitative observations extend to phase-separating materials with different transformation barrier heights, and that reducing the barrier height would increase the active particle population at lower rates. All other material parameters were kept constant.

### *Phase Separation Approximation*

Although the Li diffusional chemical potential for LiFePO<sub>4</sub> slopes downward in the two-phase region<sup>4</sup>, it is also interesting to explore the limiting case of a flat Li potential past the transformation barrier (Fig. S12). We examined this limit by specifying the Li diffusional chemical potential as a function of the average filling of each particle. We used a piecewise function to define the Li diffusional chemical potential in LFP upon discharge:

$$\mu_{Li,LFP} = \begin{cases} \Omega_a(1 - 2\bar{c}_s) + k_B T \ln\left(\frac{\bar{c}_s}{1 - \bar{c}_s}\right) & \bar{c}_s < b, \bar{c}_s > a \\ 0 & b < \bar{c}_s < a \end{cases} \quad (10)$$

where  $b$  is the spinodal point for the Li-poor compound and  $a$  is the solubility limit for the lithium-rich compound. This function resembles the chemical potential function used in recent work<sup>9-11</sup>. This approach reduced the computational time by lowering the dimension of the problem by one. Rather than solve the position-dependent lithium concentration in each particle, we solved for the average lithium fraction. We simulated 625 representative particles, with 25 electrode volumes and 25 particles in each volume.

Figure 4a plots the results of this simulation. Both the complete phase-field model and the phase separation approximation yield similar results in terms of active particle population

and current density. This shows the applicability of our conclusions for various  $\mu_{Li,LFP}$  curves for phase-separating materials.

### *Wiring Simulation*

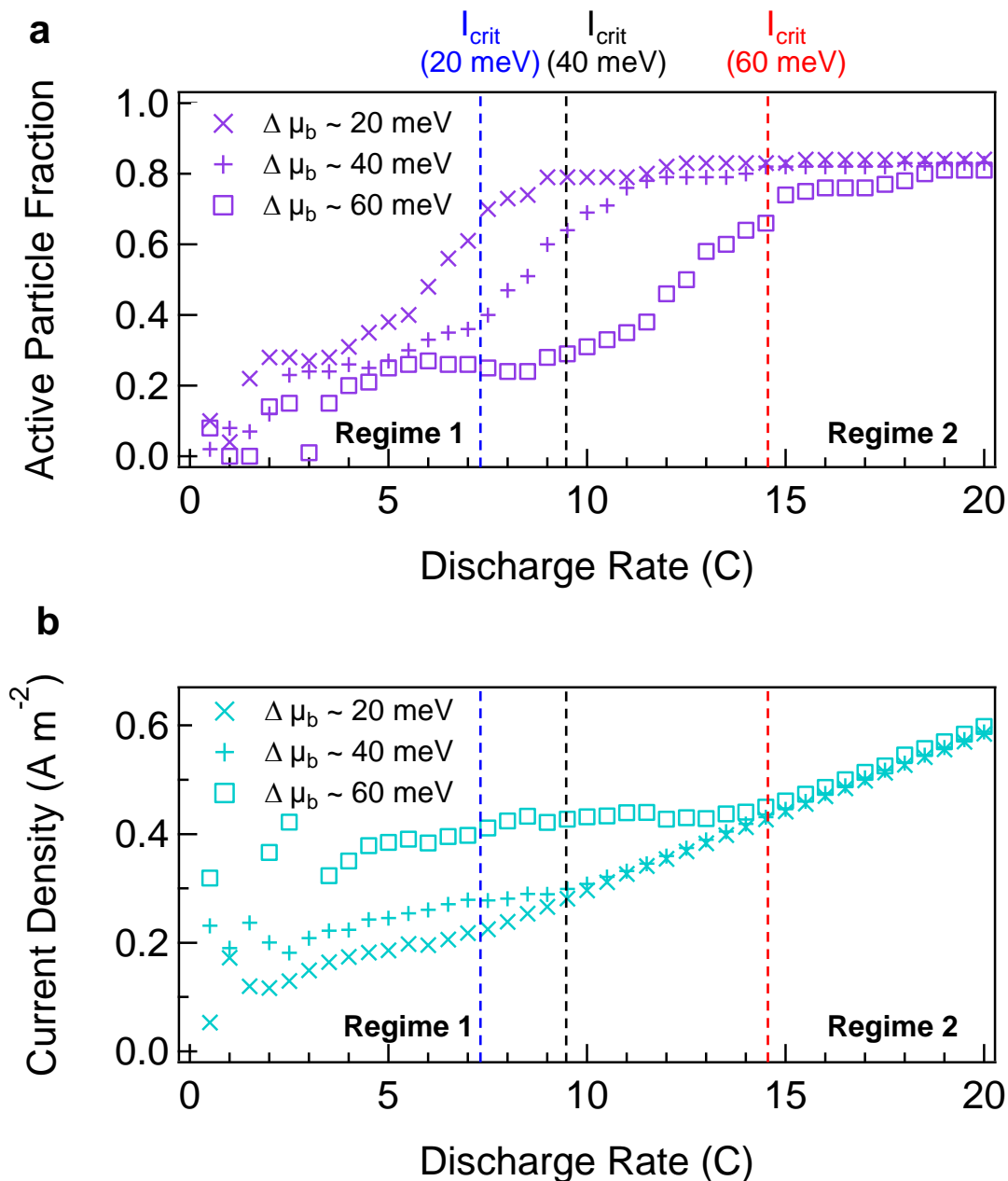
Since wiring contributes significantly to the experimentally-measured voltage (Fig. S10), we used the phase-field porous electrode model to determine if the experimentally observed active particle population arises from wiring effects, as opposed to the presence of the transformation barrier ( $\Delta \mu_b$ ). Wiring effect was simulated using an equivalent circuit model inspired by Gaberscek, Kůzma, and Jamnik<sup>12</sup>. We consider four cases: transformation barrier with zero-loss wiring, transformation barrier with highly resistive wiring, zero transformation barrier with zero-loss wiring, and zero transformation barrier with highly resistive wiring. The case presented in the main text contains a transformation barrier and zero-loss wiring. All cases considered electrolyte transport losses (Eq. S1-S5).

Figure S13 shows that either type of wiring under zero transformation barrier condition results in 100% active particle population at low discharge rates, which is inconsistent with our experimental observations. Therefore, while wiring contributes significantly to the voltage (Fig. S10), it alone cannot lead to the active particle dynamics observed in the experiments. A low active particle population and high current densities at low discharge rates appear only when the transformation barrier ( $\Delta \mu_b$ ) is included in the model.

### *Electrochemical Heterogeneities*

We also simulate the effect of heterogeneities in the electrochemical parameters. In Fig. S14, we randomized the reaction rate and exchange current density for different particles.

Despite the large variability in the reaction rate, we observe that the transformation barrier, rather than electrochemical heterogeneities, is the origin of the low active particle population at low cycling rates.



**Fig. S11: Simulated (a) active particle fraction and (b) current density for different transformation barriers.** In regime 1, the current density is determined by the barrier height

and is nearly invariant with the global electrode current; rather, the active particle fraction increases with discharge rate. In regime 2, the active particle fraction saturates and the current density is determined by the global applied current. The transformation barrier  $\Delta\mu_b$  alters the current density and active population at low rates, and reducing  $\Delta\mu_b$  could increase the current homogeneity of phase-separating particles.

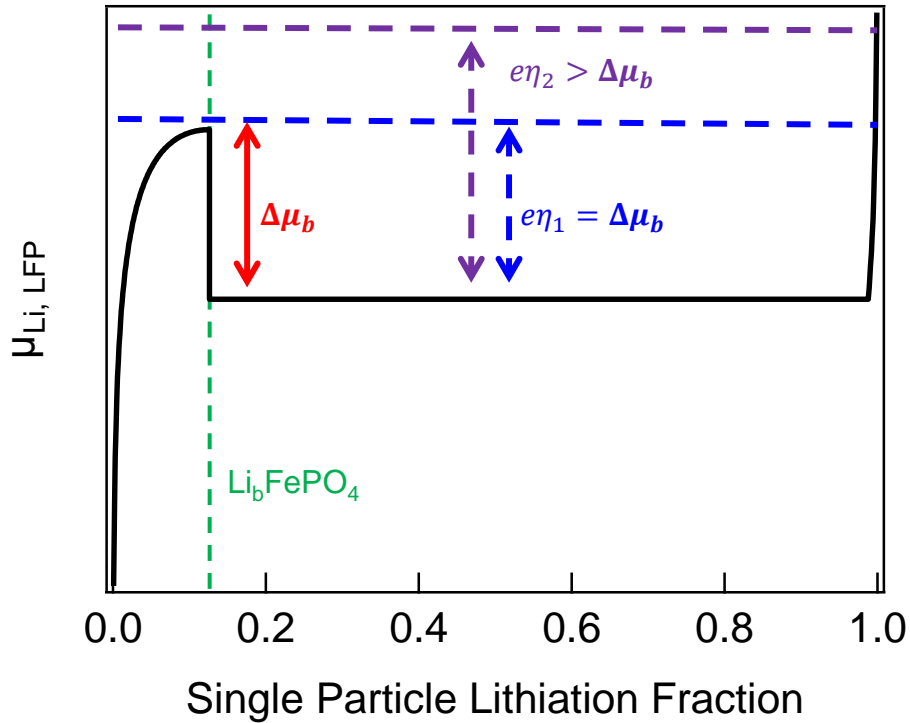


**Fig. S12: Phase-separating approximation.** The diffusional chemical potential of Li in phase-separating particles ( $\mu_{Li,LFP}$ ) also contain a transformation barrier ( $\Delta\mu_b$ ), which we take as the energy required to bring the particle from its solubility limit to the spinodal. In regime 1, the electrode accommodates extra current by increasing the active particle fraction while maintaining a constant  $\eta_1$  for intercalation at  $\Delta\mu_b/e$ . In regime 2, the active particles population

is maximized, and the electrode accommodates additional current by increasing the reaction overpotential ( $\eta_2$ ).

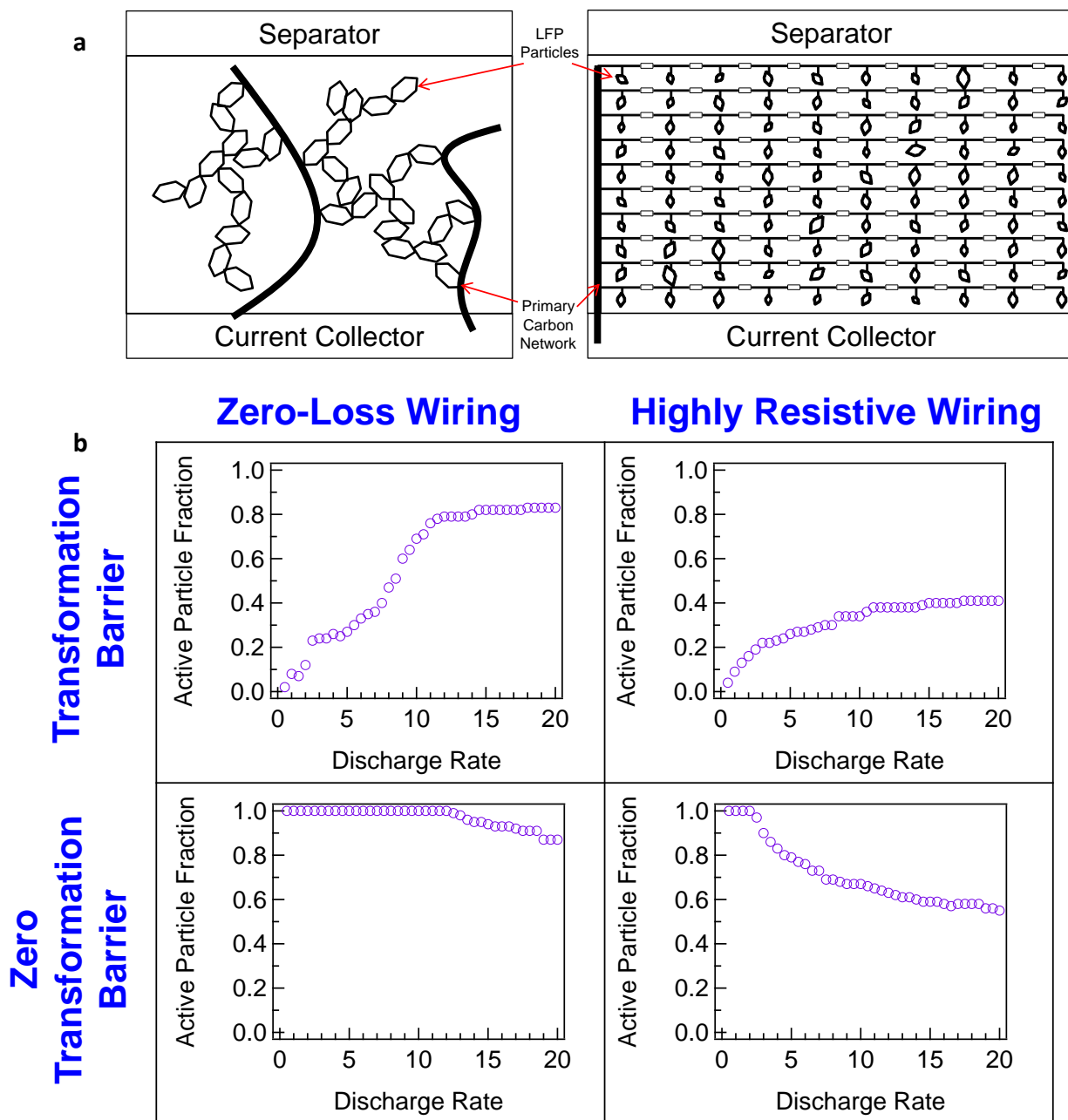


**Fig. S13: Wiring and interparticle resistance.** (a) Because we do not experimentally observe a lithiation front (Fig. S6), the wiring losses arise directly from interparticle contact resistance and

a weakly-percolating carbon network (wide black lines). We modelled highly-resistive wiring by placing a resistor between each particle; the leftmost particles are directly connected to the primary carbon network. When the wiring is highly resistive, the poorly-connected particles furthest from the carbon network would intercalate last, regardless of its distance from the current collector. To simulate a zero-barrier condition such that  $\mu_{Li,LFP}$  in LFP is monotonically increasing, we change the regular solution parameter  $\Omega_a$  to 0.

Our results in (b) show that the transformation barrier is the origin of the increase in the active particle fraction and current homogeneity with discharge rate. Highly-resistive wiring reduces the active particle population at higher discharge rates.

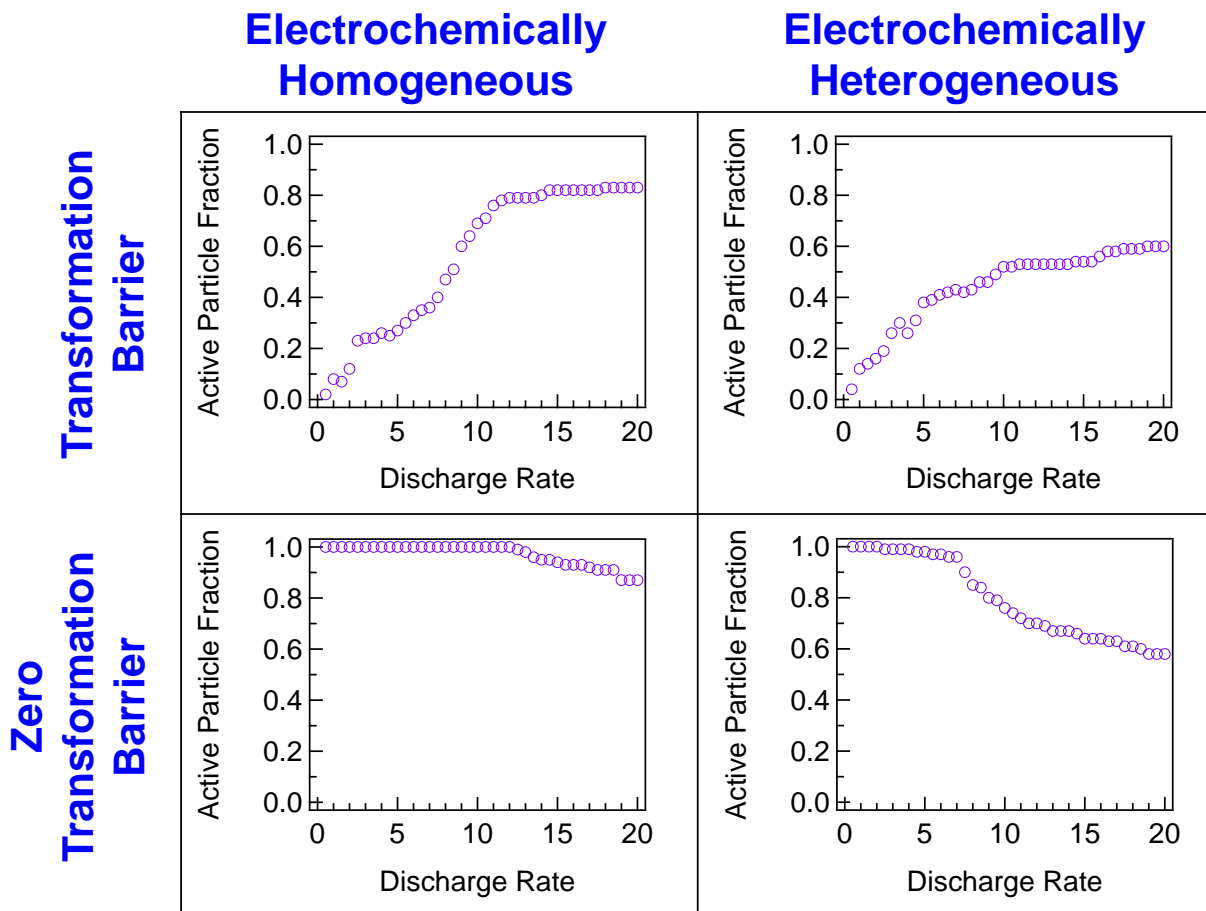




**Fig. S14: Electrochemical reaction heterogeneities.** Heterogeneity in the reaction rate constant  $k_0$  reduces the active particle population and current homogeneity at high rates. To simulate electrochemical heterogeneity, we modify the reaction rate for a particle  $k_0^*$  to be  $k_0^* = k_0 \exp(2n)$ , where  $n$  is a random number chosen from a standard normal distribution. Since each of the 100 simulated particles is assigned a different number  $n$ , the range of  $k_0^*$  spans a factor of 200. This simulation confirms that the transformation barrier, rather than electrochemical heterogeneities, is responsible for the experimentally-observed increase in active particle population with discharge rate.

**Table S1: Parameter values for numerical simulations**

Parameter	Symbol	Value	Source
Regular Solution Parameter	$\Omega_a$	$1.86 \times 10^{-20}$ J per Li	Supplementary ref. 13
Gradient Penalty	$\kappa$	$5.01 \times 10^{-10}$ J m <sup>-1</sup>	Supplementary ref. 13
Coherent Stress Penalty	$B_0$	$1.92 \times 10^8$ Pa	Supplementary ref. 13
Cation Transference Number	$t_+$	0.24	Supplementary ref. 14
Ambipolar Diffusivity	$D_{amb}$	$3.25 \times 10^{-10}$ m <sup>2</sup> s <sup>-1</sup>	Supplementary ref. 14
Lithium Site Concentration	$\rho_s$	$1.37 \times 10^{28}$ m <sup>-3</sup>	Calculated from Supplementary ref. 15
Electrode Thickness	$L_x$	60 $\mu$ m	Experimental Measurement
Separator Thickness	$L_s$	50 $\mu$ m	Experimental Measurement
Active Material Volume Loading	$L_p$	0.8	Experimental Measurement
Porosity	$\epsilon$	0.5	Experimental Measurement
Initial Electrolyte Salt Concentration	$c_0$	1.2 M $\sim 7.23 \times 10^{26}$ m <sup>-3</sup>	Experimental Measurement
Electrode Surface Area	$A_{cell}$	2.0 cm <sup>2</sup>	Experimental Measurement
Temperature	$T$	298 K	Room Temperature

## Supplementary References

1. Hitchcock, A. aXis 2000 is written in Interactive Data Language (IDL), 2008. It is available free for non-commercial use at <<http://unicorn.mcmaster.ca/aXis2000.html>>
2. Chueh, W. C. *et al.* Intercalation Pathway in Many-Particle LiFePO<sub>4</sub> Electrode Revealed by Nanoscale State-of-Charge Mapping. *Nano Lett.* **13**, 866–872 (2013).
3. Ferguson, T. R. & Bazant, M. Z. Nonequilibrium Thermodynamics of Porous Electrodes. *J. Electrochem. Soc.* **159**, A1967–A1985 (2012).
4. Cogswell, D. A. & Bazant, M. Z. Theory of Coherent Nucleation in Phase-Separating Nanoparticles. *Nano Lett.* 3036–3041 (2013).
5. Smith, K. C., Mukherjee, P. P. & Fisher, T. S. Columnar order in jammed LiFePO<sub>4</sub> cathodes: ion transport catastrophe and its mitigation. *Phys. Chem. Chem. Phys.* **14**, 7040–7050 (2012).
6. Ferguson, T. R. *Lithium-ion Battery Modeling Using Non-equilibrium Thermodynamics*. Doctoral thesis, Massachusetts Institute of Technology (2013).
7. Bazant, M. Z. Theory of Chemical Kinetics and Charge Transfer based on Nonequilibrium Thermodynamics. *Acc. Chem. Res.* **46**, 1144–1160 (2013).
8. Bai, P. & Bazant, M. Z. Charge transfer kinetics at the solid-solid interface in porous electrodes. *Nature Commun.* **5**, 3585 (2014).
9. Bai, P., Cogswell, D. A. & Bazant, M. Z. Suppression of phase separation in LiFePO<sub>4</sub> nanoparticles during battery discharge. *Nano Lett.* **11**, 4890–6 (2011).
10. Dreyer, W. *et al.* The thermodynamic origin of hysteresis in insertion batteries. *Nature Mater.* **9**, 448–453 (2010).
11. Sasaki, T., Ukyo, Y. & Novák, P. Memory effect in a lithium-ion battery. *Nature Mater.* **12**, 569–575 (2013).
12. Gaberscek, M., Kuzma, M. & Jamnik, J. Electrochemical kinetics of porous, carbon-decorated LiFePO<sub>4</sub> cathodes: separation of wiring effects from solid state diffusion. *Phys. Chem. Chem. Phys.* **9**, 1815–1820 (2007).
13. Cogswell, D. A. & Bazant, M. Z. Coherency strain and the kinetics of phase separation in LiFePO<sub>4</sub> nanoparticles. *ACS Nano* **6**, 2215–2225 (2012).
14. Nyman, A., Behm, M. & Lindbergh, G. Electrochemical characterisation and modelling of the mass transport phenomena in LiPF<sub>6</sub>–EC–EMC electrolyte. *Electrochim. Acta* **53**, 6356–6365 (2008).

15. Padhi, A. K., Nanjundaswamy, K. S. & Goodenough, J. B. Phospho-olivines as Positive-Electrode Materials for Rechargeable Lithium Batteries. *J. Electrochem. Soc.* **144**, 1188–1194 (1997).